

16.343 : Spacecraft and Aircraft Sensors and Instrumentation

Term Project Report 6

Sreeja Nag

Instrument: Visible and near IR, medium-resolution, Matrix Imaging Spectrometer for nanosatellites

Objective: To make multi-angular, multi-spectral passive radiance measurements of the same ground target at the same time using a cluster of nanosatellites in formation flight

Table of Contents

1. Introduction	1
1.1. Current Technologies	2
1.2. Motivation	4
2. Approach	5
2.1. System-level Payload Modeling	5
2.2. Measurement Goals	8
2.3. Functional Mapping of Goals to Requirements	9
3. Instrument Selection and Design	17
3.1. Waveguide Spectrometers	19
3.2. Acousto-Optic Tunable Filter Spectrometers	22
3.3. Integral Field Spectrograph	24
3.4. Mapping of Functional Requirements to Instrument Form	25
4. System Testing	26
4.1. Calibration Methods	26
4.2. Test Plan	28
5. Risk Assessment	29
6. Conclusions	30
7. List of Acronyms	31
8. References	31

1. Introduction

This report focuses on the development of a payload for a science mission aimed to perform measurements for the estimation of full bidirectional reflectance distribution function (BRDF) of sampled ground/water/cloud pixels. BRDF describes the properties of anisotropically scattering surfaces in the reflection of solar incident light [1]. It provides a way of geometrically and quantitatively expressing the connection between radiance reflected from a ground pixel in a given direction and the incident irradiance arriving at that pixel from some other direction [2]. BRDF is needed for correction of view angle and illumination angles in image standardization, derivation of surface albedo [3], climate modeling and the calculation of radiative forcing at the top of the atmosphere [4], land cover classification, cloud detection and atmospheric corrections [1]. BRDF measurements are needed in the retrieval of albedo and aerosol optical properties [24] and are useful in determining thermal anisotropy, Normalized Difference Vegetation Index (NDVI), land surface temperature and leaf area index (LAI) [5]. Furthermore, it is important to measure it with high enough temporal frequency and spatial scale so that instantaneous reflected flux can be correlated with specific phenomena such as tropical storms [4].

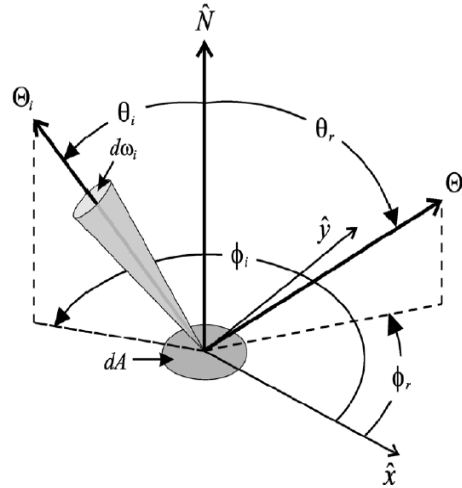


Figure 1: BRDF view and illumination angle geometry. The positions of the imager and the sun relative to the target are conventionally represented by three angles known as the zenith viewing angle (Θ_r), the solar zenith angle (Θ_i) and the relative azimuth angle ($\phi_i - \phi_r$)

Figure 1 shows the typical BRDF measurement geometry. Since BRDF measurements require measurement of radiance from multiple angles at the same time from the same ground pixel, it is impossible to do it using the same satellite. The measurement gap between what we want and what we can get using a single satellite is further expressed in Figure 2 for a cloud pixel (not to scale). The figure shows that a single satellite can make measurements only along a restrictive plane (orbital plane for forward aft looking sensors and scan plane for scanning sensors) and those measurements too are separated by a few minutes. In areas of high environmental variability such as tall tropical clouds, this time is enough to change the target. Therefore, the best (and in fact, the only way) of measuring radiance in order to determine BRDF with sufficient variation in all 3D angles shown in Figure 1 is through the use of multiple satellites or a distributed satellite system.

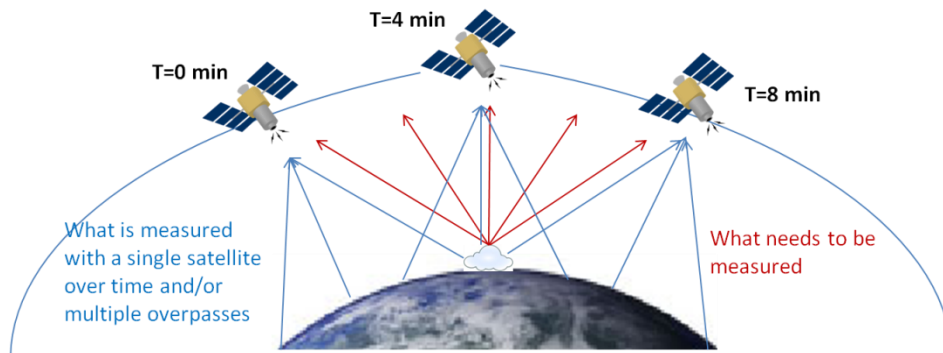


Figure 2: Limitations of the measurements a single satellite is capable of making (blue) versus measurements required for BRDF estimation (red). ‘T’ represents nominal time differences that a LEO satellite takes to make the given measurements. Therefore, the need for multiple satellites for BRDF measurements.

1.1. Current Technologies

The main science goals for BRDF mission are:

1. Radiance measurements across *multiple angles* (azimuth and zenith measurement angles as well as solar zenith angles; samples on the solar principal plane specially in the backscatter direction)
2. Radiance measurements across *multiple wavelengths* (large spectral range, high spectral resolution)

3. Frequent *repeat* of the ground track
4. Medium to High *spatial resolution*

Multi-angular and multi-spectral measurements have been traditionally done using spaceborne and airborne instruments.

Spaceborne BRDF products in the present and past have not been able to densely sample the BRDF polar plot for any location because their repeat passes over a ground spot span over days and a spacecraft with one fixed sensor can take only one sample at every overpass. Nonetheless, missions have tried to maximize their angular data by combining their measurements over multiple overpasses, assuming that the ground BRDF and atmospheric properties remain relatively stable over time during this period (not always true). The sensors collect angular data by virtue of having a very wide field of view in the along and/or cross track direction so the same point appears in different positions in the swath hence difference angles (e.g. MODIS, AVHRR, NPOESS VIIRS) or multiple sensors pointing in different directions or a variably pointing instrument in the forward-aft direction (e.g. MISR, ATSR). Even so, the range of angular variation is very narrow and results extrapolated onto the important but unsampled principal plane (PP) may have errors up to 40-50% [6]. The large swath may also cause the resolution to be coarse [7]. Table 1 compares the main spaceborne instruments with BRDF products in the present with respect to the above requirements. Note that the ground pixel resolution is dependent on the imaging wavelength. Other instruments such as Landsat, SPOT-HRV (31.13° CT scan angle) and AVHRR (3000 km swath due to 70° view zenith angles) also have BRDF products but they are even more limited angular and spectral coverage than those in Table 1.

Requirements → Instruments ↓	Repeat period of coverage (any view) in days	Ground Pixel Size in km X km	Spectral Range	# of spectral bands	Number of angles (PP = Principal Plane, P = Polarization)
MODIS [8]	~2 (16day RGT)	0.25-1	0.4-14.4 μm	36	N/A
MISR [9]	9	0.275 X 1.1	0.44-0.87 μm	4	9
ATSR [10][11]	3-4	1 X 2	0.55–12 μm	7	2
ASTER [6]	No repeat	0.15 X 0.9	0.52–11.65 μm	14	2
SPECTRA [12]	14	0.5 X 0.5	0.45–12.3 μm	62	7/PP
POLDER [13]	~2 (16day RGT)	6 X 7	0.42-0.9 μm	9	14/PP/P
CHRIS [14][15][7]	110 day RGT	0.17-0.5	0.415-1.05 μm	18-63	15/PP
CERES [16][17]	2	10 - 20	0.3-12 μm	3	N/A

Table 1: Comparison of current spaceborne mission instruments in terms of BRDF specific requirements. Red highlights indicate incomplete engineering requirements for achieving BRDF science objectives

Airborne BRDF products are available from various instruments as documented in Table 2, as discussed in an interview with NASA GSFC experts [18]. The instruments do not fall short of any requirements in absolute terms except “repeat period”, hence Table 1 does not have any red boxes. The instruments represent the state of the art measurements for BRDF estimation and will be used to define the science and measurement goals of the nanosatellite BRDF mission. The Cloud Absorption Radiometer (CAR), which was developed at NASA Goddard Space Flight Center (GSFC), is considered a heritage instrument for BRDF and will be referenced most of all.

Instrument Name	Airborne Platforms	Instantaneous Field of View	Swath Width	Spectral Range	# of spectral bands	Capability (TIR = Thermal IR, P = Polarization)
CAR [1]	Douglas B-23, J-31, CV-580, P-3B, C-131A	17.45 mrad	190°	0.34-2.3 μm	14	N/A
AVIRIS [19]	ER-2, WB57, Proteus, Twin Otter	1 mrad	30°	0.38-2.5 μm	224	N/A
E/MAS [20]	ER-2	2.5 mrad	85.92°	0.44-14.24 μm	50	TIR
MASTER [21]	B-200, ER-2, Caravan, WB-57, DC-8	2.5 mrad	86°	0.44-13.00 μm	50	TIR
RSP [22]	J-31, P-3B	14 mrad	121°	0.41 – 2.25 μm	9	PP
SSFR [23]	Proteus, Twin Otter, J-31, DC-8, P-3B,	Hemispheric		0.38 – 2.2 μm	175	N/A
AIRMISR [24]	ER-2	0.3 mrad	29.8°	0.44 – 0.86 μm	4	N/A

Table 2: Comparison of current airborne mission instruments, representative of state-of-the-art BRDF estimations, in terms of BRDF specific requirements

Existing spaceborne measurements for estimating BRDF, although global, have *gaps* in at least one or more important requirements for a full BRDF estimation – *red boxes in Table 1*. Most instruments even over a full repeat cycle have not been able to image the angular spread of possible anisotropy. For example, MODIS has a period of 100 minutes, however to make a triplet measurement, that is 3 angular measurements, which is the minimum that some BRDF models need, will take at least 4 hours because the measurements are cross-track, which may be too long a period to study highly varying tropical clouds or other tropical phenomena. The newer instruments such as the CHRIS and POLDER have achieved more angular spread but at the cost of global coverage or spatial resolution. Thus, even with high masses and costs, they have missed out on many scientific interpretations that airborne instruments like CAR have been able to make. However, airborne instruments can only make measurements locally for specific areas and temporally concentrated over a few hours or days. They cannot capture variability in atmospheres over continents over the scale of, say, tropical cloud development (~1-2 days) and the cost per unit area per unit time is very large. Additionally, all the spaceborne instruments mentioned in this section are nearing their end of life, in fact, Terra carrying MODIS and MISR has already overshoot its life by 6 years. With the exception of the JPSS satellites that will carry the VIIRS sensor (already being flight-tested on the NPP satellites) capable of multi-angular imaging by virtue of its large swath and the CERES instrument, there are no large scale BRDF projects in the pipeline. Due to programmatic changes and cancellation of the NPOESS program, JPSS will likely not be operational before 2017, if not later. This leaves a gap in BRDF measurements after the current generation of instruments die out and the newer ones come in.

1.2. Motivation

Clusters and constellations of multiple nanosatellites in formation flight carrying identical VNIR (visible and near infrared) and possibly SWIR (short wave infrared), medium-resolution spectrometers as payloads can be used to make BRDF measurements. Collectively, they can make radiometric measurements at multiple angles and bands and also are capable of providing global, temporal coverage is therefore fill in the gap in BRDF estimations. More

importantly, they are indispensable for filling the gap of generation transitions between large instruments because of their low cost, resilience to risks and low time of development. The angular spread and global coverage of the measurements will depend on the cluster geometry, orbits and attitude control, as discussed in a separate study [25], which in turn constrain the altitude of the nanosatellites, their nadir viewing angles and swath requirements to account of attitude errors. This report will discuss the development of the payload for the nanosatellite buses.

Recently, nanosats and Cubesats have been successful in doing radiometric science over and above being technology and educational demonstrations. MicroMAS is a hyperspectral microwave radiometer developed by MIT/LL [26] using a high frequency passive radio receiver. VNIR hyperspectrometers for small satellites have been successfully demonstrated in Japan “Taiki” [27] using a Ritchey-Chretien telescope and COTS-obtained CCD image arrays. Aalto-1 is a 400g spectral imager based on a tunable MEMS or piezo-actuated Fabry-Perot Interferometer developed by Aalto University in Finland. Far-IR radiometers based on microbolometers using many options of materials have been developed and tested [28][29]. CanX-2 carries an atmospheric spectrometer, Cloud CubeSat a VIS/NIR camera and a polarimeter and QuakeSat a ULF signal sensor [30]. All these successful small satellite, scientific projects have paved the path for the miniaturization of telescopes as well as visible to infrared detectors using CCD or CMOS arrays, SWIR or FIR thermal detectors, usage of dichroic filters or gratings to disperse the different wavelengths of incident light, on-orbit calibration techniques using infrared lasers/illumination lamps/natural sources. Therefore, while development of the payload for the BRDF nanosatellites seems to be challenging, there are past resources that can help constructively in informing the process.

2. Approach

BRDF will be estimated from radiance measurements taken by multiple nanosatellites, each with an identical spectrometer, in a cluster sensing the same ground pixel at the same time. The boresight and azimuthal angle of each satellite sensor with respect to the ground pixel, area of the ground pixel and the required attitude control is calculated from the various proposed cluster geometries, their sizes and altitudes [25]. The altitude range considered for the nanosatellites is 500 km to 800 km (LEO) for which the boresight angle range available (different for different geometries) is 0° to 60° . A payload systems model will be used to estimate the dependence of the optical parameters (front end of the payload) and the system metrics on the design variables. These variables have been obtained from either BRDF science requirements derived from heritage airborne missions [1] or from the cluster geometry model. The trades of these variables will provide acceptable ranges of optical parameters will then be used to design a miniaturized spectrometer. It will be shown that matrix imaging best mitigates the risks of system attitude errors. Three spectrometer types have been proposed for 2D spatial and 1D spectral imaging along with a CCD array of Silicone and InGaAs diodes as the detectors.

2.1. System-level Payload Modeling

The spectrometer payload system has been modeled using several design variables leading to important system metrics (red) and optical system determinants (green) as shown in Figure 3. The design variables include boresight angles and altitude from the cluster geometry model and other variables derived from BRDF airborne instruments which include wavelength of radiation considered (UV to SWIR that is 300nm to 2300 nm), ground pixel length (200 m to 1 km) and bandwidth (10 nm to 40 nm). The bandwidth is a system metric because it depends on the efficiency of the spectrometer to split the incoming light. The variation of bandwidths with

wavelength of the CAR instrument will be shown in a later section. The payload model will allow us to assess the dependence of metrics - expected signal to noise ratio (SNR) and swath - on the design variables as well as map how both affect the high level optical system parameters – pixel size, focal length, aperture diameter, number of pixels and spectral bands.

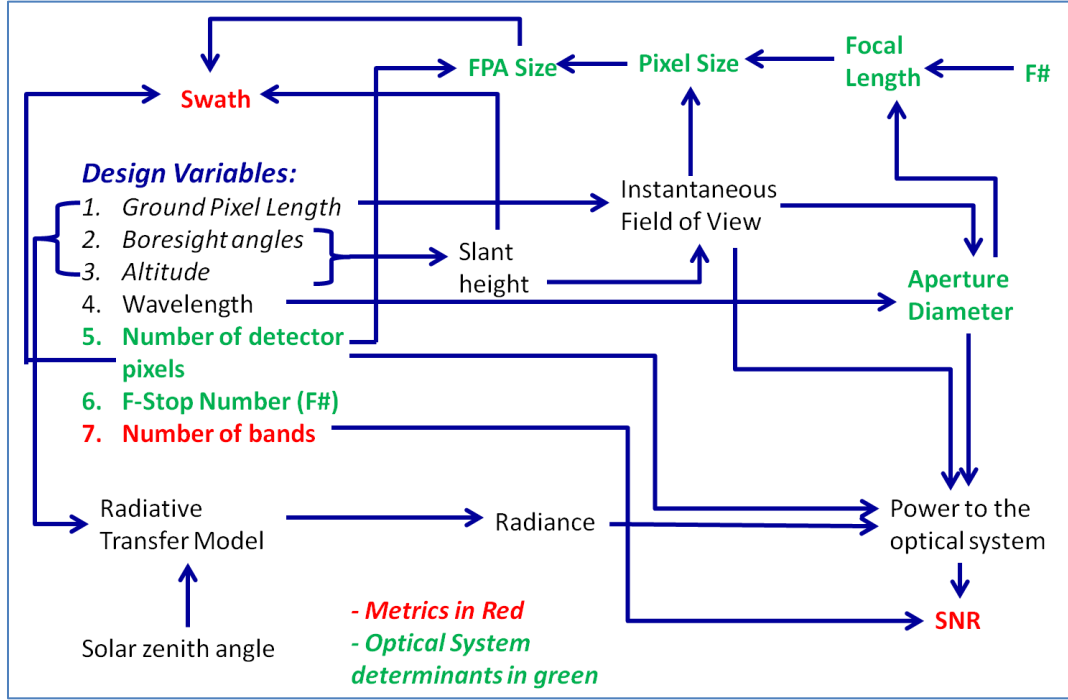


Figure 3: Payload Modeling Overview. System metrics are highlighted in red and intermediate variables affecting the optical system in green. Italicized design variables indicate those derived from the cluster geometry model

As shown in Figure 3, instantaneous field of view (iFOV) depends on the boresight angles (η), altitude (h) and ground pixel size (gps) by Equation 1 through Equation 5[31]. D is the slant distance between the sensor and the ground pixel, λ is the earth central angle, ε is the elevation angle and ρ is the boresight angle at the horizon – all angular variables shown in Figure 4.

$$iFOV(gps, alt, \eta) = \sin^{-1} \left(\frac{gps}{D(alt, \eta)} \right)$$

Equation 1

$$D(alt, \eta) = alt \quad \forall \eta = 0$$

$$D(alt, \eta) = R * \frac{\sin(\lambda)}{\sin(\eta)}$$

Equation 2

$$\lambda = 90 - \eta - \varepsilon$$

Equation 3

$$\varepsilon = \cos^{-1} \frac{\sin(\eta)}{\sin(\rho)}$$

Equation 4

$$\rho = \sin^{-1} \frac{R}{R + h}$$

Equation 5

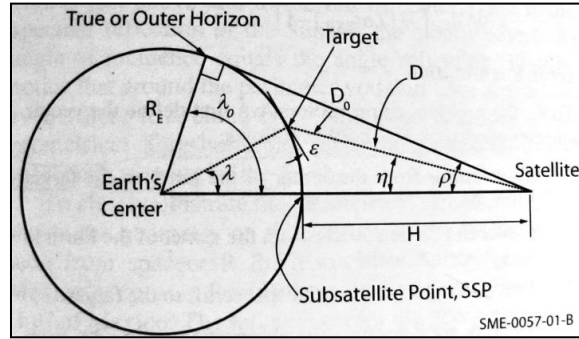


Figure 4: Definition of angular relationships between the satellite, target and Earth's center as shown in [31]

Instantaneous field of view (iFOV) varies is dependent on all three design variables: altitude (h) and boresight angle (η , through slant distance) and the ground pixel size (gps). IFOV required for a given gps clearly decreases with increasing altitude and this is more pronounced at larger nadir angles due to large increases in the slant distance with increasing altitude. IFOV required for a given nadir angle increases by relaxing the resolution requirement (gps), more so for vertical viewing than tangential. Given the wavelength of radiation and iFOV, the diffraction limited aperture diameter can be calculated. For an F# of 1.5 (derived from heritage instruments with BRDF products) focal length and then, for one detector pixel per ground resolution element, the required pixel size can be calculated. For a selected and constant aperture diameter, the diffraction limited spot size for lower wavelengths will be much smaller than higher ones. Therefore, the diffraction limited pixel size calculated from near-IR will limit the resolution available to UV 'for the same aperture diameter. For different wavelength bands, it is possible to calculate the pixel size from the F# for finer sampling of those bands. The F# has also been varied to show its dependence on the focal length and pixel-size later. The number of detector pixels requirement constrains the swath and the focal plane array size.

Signal to noise ratio (SNR) is one of the most important metrics for determining the value of the optical system. It is calculated by integrating the radiance at a given altitude over the area of the aperture and integrative time (dependent on the ground velocity). Radiance can be estimated using an atmospheric radiative transfer model e.g, SBDART from the UCSB or COART from NASA Langley or available datasets from existing missions, examples being MODIS, MISR, POLDER. The Coupled Ocean Atmosphere Radiative Transfer (COART) model [32], a publicly distributed software for radiative transfer by NASA, was used to calculate the radiance in $\text{W/m}^2/\text{sr}/\mu\text{m}$ at an altitude of 100 km (the highest available) for different solar zenith angles (SZA), sensor boresight angle (η) and wavelength of radiation (λ). This radiance can be integrated over the aperture area, wavelength bandwidth and solid angle of the field of view (FOV) to calculate the power received by the optical system. SNR is a function of this received power and is dependent on the spectrometer type.

Figure 5 shows the COART model radiances as \log_{10} for $\text{SZA} = 0^\circ, 40^\circ, 80^\circ$. The maximum and monotonically increasing variation is seen for the visible (400-700 nm) and NIR (700-1400 nm). There is a drop in radiance in the UV and SWIR regions. Increasing SZA angles leads to more outward radiance because the earth radiates more during sunset than noon. The boresight angle dependence is very little compared to dependence on wavelength and SZA, however, it becomes more important with higher SZA. It is important to note, though, that the COART model has been developed to match available sensor data and, as shown in Section 1, hardly any missions have successfully sampled the boresight angular variation of radiance therefore the variation with respect to angles may be underrepresented in these charts. The numbers are intended only for nominal calculations of expected SNR to

design the payload. Since there is nothing significant to affect the radiation transfer above 100 km, the radiance measured at 100km can be assumed to be the same at LEO altitudes¹.

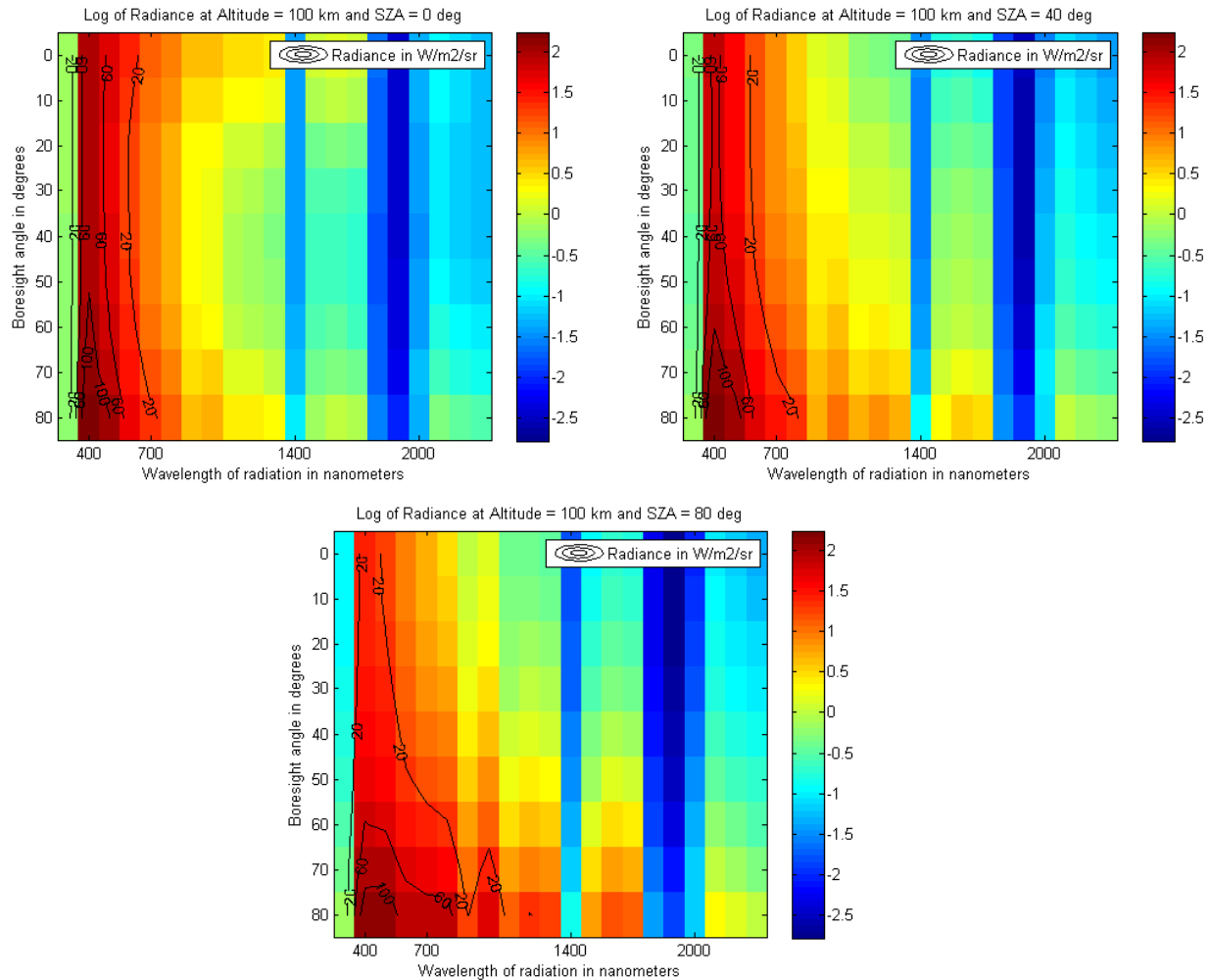


Figure 5: Radiance at 100 km altitude as provided by the COART model for atmospheric radiative transfer for varying sensor boresight angles and radiation wavelength, for solar zenith angles of 0°, 40°, 80° as a heat map

The COART model results show the range of variation of radiance dependent on the time of the day as well as the atmospheric transmission windows. This knowledge will help determine the wavelength band limits in the spectrometer so that the measurements are within the radiometric range of the detectors for those bands.

2.2. Measurement Goals

Given the angular, spectral, spatial and spectral requirements of the BRDF mission, the *measurement goals for the nanosatellite spectrometer* can be summarized as:

¹ Confirmed via an email conversation with Dr. Zhonghai Jin, the primary programmer of the COART model

1. Radiance measurements at a range of altitudes – 500km to 800km
2. Radiance measurements at a range of nadir viewing angles – 0° to 60°
3. Radiance measurements at a range of solar zenith angles – 0° to 80°
4. Spatial resolution at a range of ground resolution lengths – 200 m to 1 km
5. Spectral measurements over a range of wavelengths – 300 nm to 2300 nm
6. At least 14 spectral bands are required (derived from the CAR instrument [1]) at the wavelengths and bandwidths shown in Figure 6. Since the current instrument being designed is a spectrometer, the band numbers and widths will be dependent on parameters such as detector types, free spectral range and radiometric range but the CAR values will be used as reference
7. Measurements will be collected only during daylight
8. Maximize swath to ensure overlap of ground pixels of the whole cluster
9. Maximize signal to noise ratio (SNR)

Items 2, 3 and 4 are metrics that come from feasible geometries of the BRDF cluster (in italics in Figure 3). The spectrometer optical, dispersion and detector system requirements will be defined on the basis of these measurement goals after a detailed tradespace analysis.

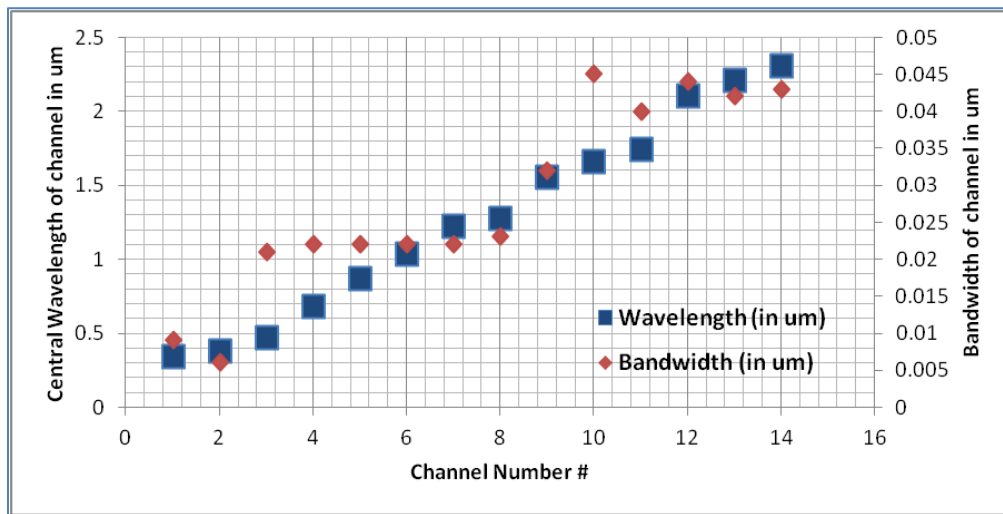


Figure 6: Wavelength requirements for the imaging spectrometer based on the Cloud Absorption Radiometer airborne instrument [1]

2.3. Functional Mapping of Goals to Requirements

The relationships in Figure 3 can be used to map some of the measurement goals to optical system requirements (green) and metrics (red).

Selection of the wavelength bands for the spectrometer depends on the following criteria: Free spectral range of the central wavelength, spectral range of detectors available and radiometric range of detectors available. To prevent the overlap of one dispersive order of a wavelength with the lower order of a higher wavelength, no band can contain an integral multiple of a wavelength it contains [33]. Silicon detectors work best between 350 nm to 1000 nm while InGa, InAr or GaAs detectors work best for the NIR to short wave IR range of 1000 nm – 2500 nm [34]. Finally, the power received by any detector should not vary by more than the square root of its order –

this is based on the assumption that the random noise in the detector can at most be the square root of its maximum signal which can at most be the detector's well capacity.

Optimizing all the requirements gave the following band distribution – listed in Table 3 and shown figuratively in Figure 7. Four wavelength bands are proposed, that is, the incoming light would need to be split into these four ranges using dichroics as shown in Figure 8, bounds and central wavelength corresponding to Table 3 and bandwidth of the individual bands within each range monotonically increasing with wavelength. Figure 7 thus shows that longer wavelengths have more spread out wavelength bands. Bandwidths have been chosen with reference to the CAR instrument and to compensate for the drop in radiance energy with increasing wavelength and thus operate within acceptable radiometric range. The resolution required of each dispersive element can be calculated from Equation 6 where the variables correspond to Table 3.

$$R = \frac{\Delta\lambda}{\delta\lambda} = \frac{\text{Wavelength Bound 2} - \text{Wavelength Bound 1}}{\text{Bandwidth}}$$

Equation 6

Range #	Wavelength Bound 1 (nm)	Wavelength Bound 2 (nm)	Central Wavelength (nm)	Bandwidth (nm)	Resolution (R)
1	350	650	500	10	30
2	650	950	800	20	15
3	950	1850	1370	30	28
4	1850	2310	2050	40	13

Table 3: Potential wavelength bands for the proposed spectrometer

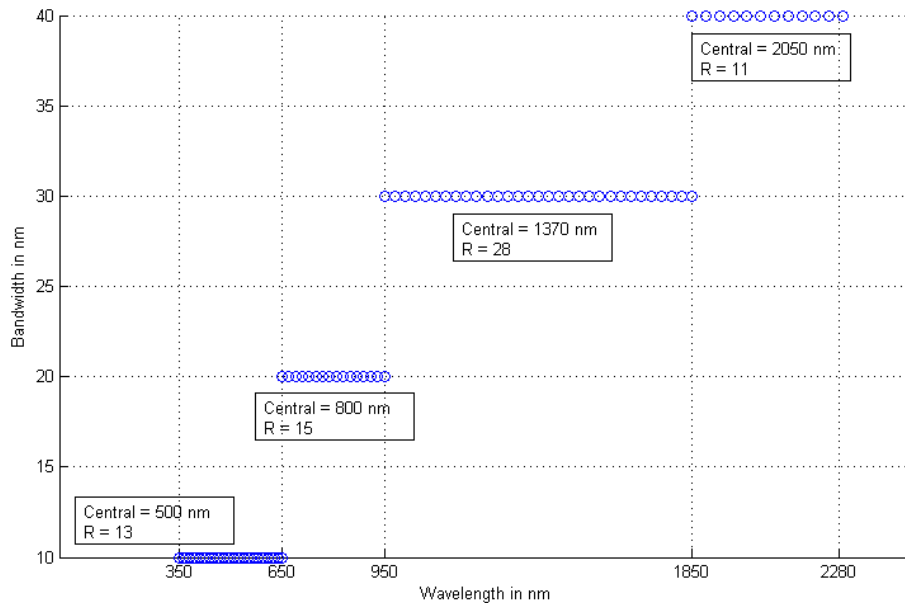


Figure 7: Proposed wavelength bands for the spectrometer and their corresponding bandwidths. The boxes show the central wavelength and resolution ($R = \Delta\lambda/\delta\lambda$) for the 4 bands.

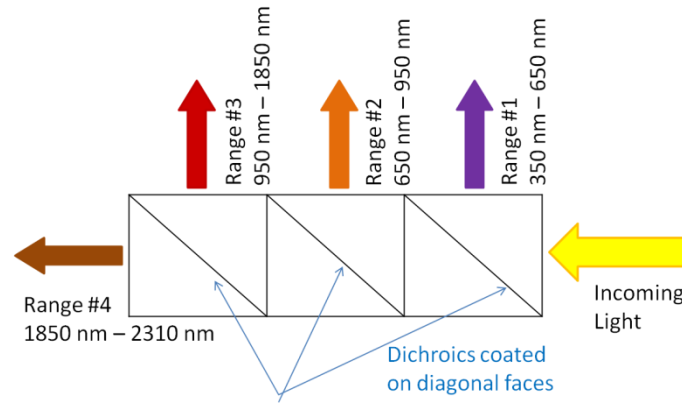


Figure 8: Proposed design for producing 4 wavelength bands for input into 4 dispersive elements, achievable in a small volume of [1" x 0.5" x 0.5"]

Assuming the highest wavelength to be 2300 nm, Figure 9 shows the variation of the required focal length (plotted as log10 to exaggerate the variation for larger ground pixels) and aperture diameter (contoured in bold black) for altitudes of 500 km and 800 km. Slant distances to the ground pixel (D) have been contoured in plain black. The highest focal lengths and diameters are needed for highest angles, slant distances and resolutions (tightest iFOV requirements) which are the Pareto utopia points. Thus for Pareto optimal performance, the diameter can be baselined at $10^{0.7} = 7$ cm and the focal length = 10.5 cm for a constant F# of 1.5 – which are all feasible in nanosatellites or 6U cubesats. The assumption of constant F# will be changed and the effects of its variation will be shown later in the section.

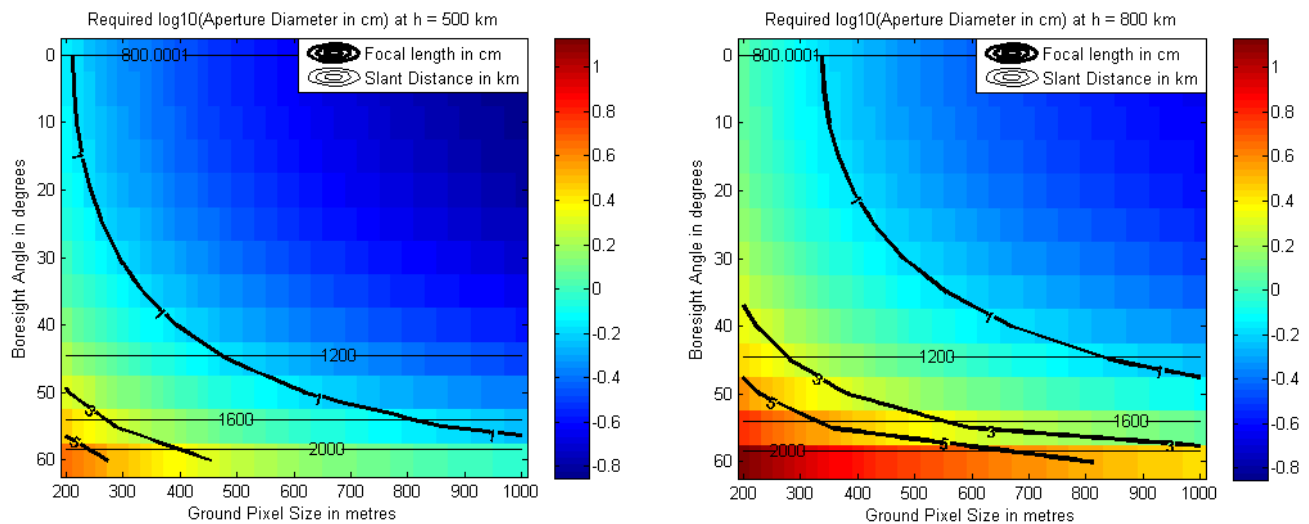


Figure 9: Variation of required focal length (as log10) at altitudes = 500km, and 800 km over boresight angle to the ground pixel and ground resolution. The corresponding required aperture diameter and the slant distances for the boresight angles are contoured. The best design is on the bottom right corner of the right panel.

Assuming the baseline diameter of 7 cm, focal length of 10.5 cm and one pixel on the FPA per ground resolution element, the required pixel size can be calculated as a function of boresight angle, altitude and ground resolution. Combining the first 2 variables into one, Figure 10 – left panel - shows the required pixel size as a function of

slant distance (function of altitude, boresight angle and elevation) and ground resolution. The right panel shows the dependency of slant distance on elevation angle therefore causing the oscillatory characteristic of the graph with sharp transitions.

Figure 10 shows that the smallest pixels are needed for highest angles, slant distances and resolutions (tightest iFOV requirements) which are the Pareto utopia points. Thus for Pareto optimal performance, the pixel size can be baselined at 20 μm for one pixel per ground pixel for diffraction limited imaging at 2300 nm. Since the diffraction limited spot size decreases with wavelength, as given by Equation 7, more resolution is achievable (for the same aperture diameter of 7 cm) on the FPA than 20 μm if the pixel size is make smaller.

$$dp = 1.22 * \lambda * F\#$$

Equation 7

The pixel sizes required to operate at the respective diffraction limits of the central wavelengths of the four potential instrument bands (500 nm, 800 nm, 1370 nm, 2050 nm) are calculated from Equation 7 and relaxed to be 1 μm , 1.5 μm , 3 μm and 4 μm . Thus, while 20 μm is the maximum pixel size that will fit the Rayleigh resolution criteria for the longest wavelengths, 1 μm , 1.5 μm , 3 μm and 4 μm are the minimum pixel sizes required to resolve as low as the diameter allows for the 4 selected wavelength ranges.

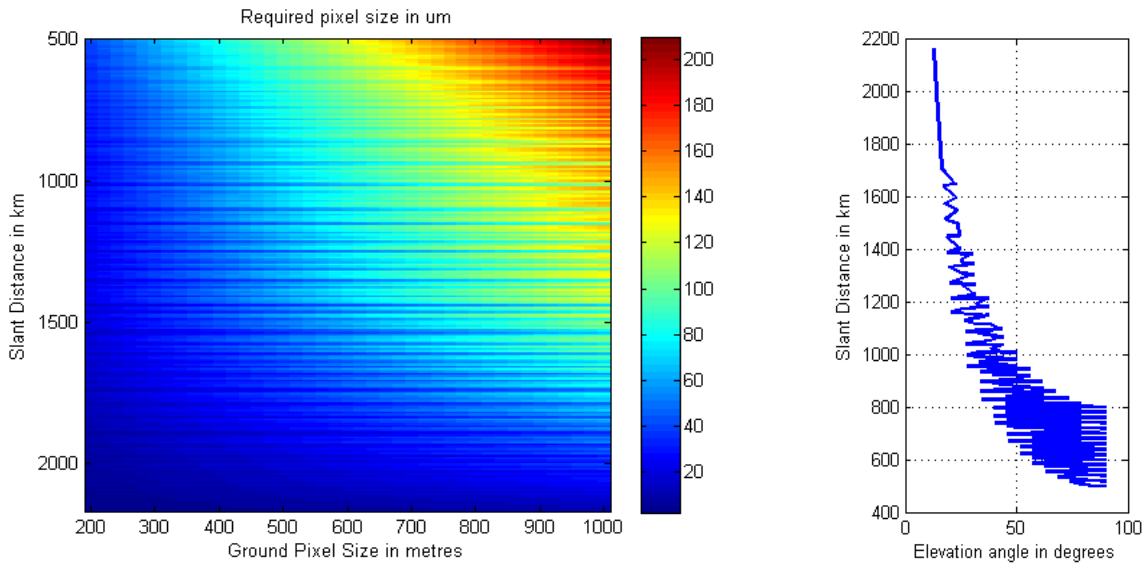


Figure 10: Required pixel size on the Focal Plane Array (FPA) as a function of slant distance (function of altitude, boresight angle and elevation) and ground resolution. The oscillatory characteristic is due to the dependence on elevation. The best design is on the bottom right corner of the left panel.

Figure 11 shows that varying the F# number or the lens speed of the camera changes the required focal length of the system (marked in magenta) and the required pixel size to resolve upto the diffraction limit of every wavelength range (marked in all other colors). An F# of 1.5, as assumed in the previous trades, needs a focal length of 10.5 cm which is achievable in 6U cubesats but if a further focal length reduction is required, the shutter or lens needs to be slower. Aside of engineering complexity, the trade-off is that the detector pixel sizes need to be even tighter to maintain the same resolution.

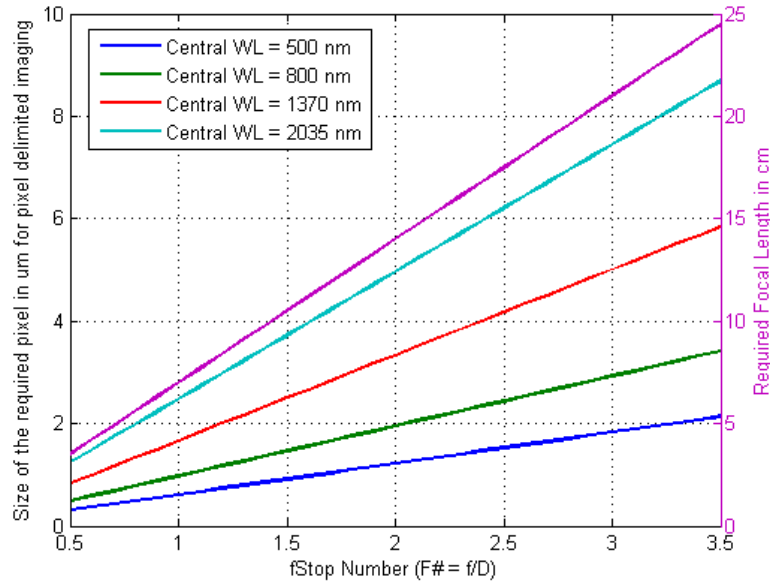


Figure 11: Dependence of pixel size required to achieve pixel-delimited resolution and focal length on F# for an aperture diameter of 7 cm.

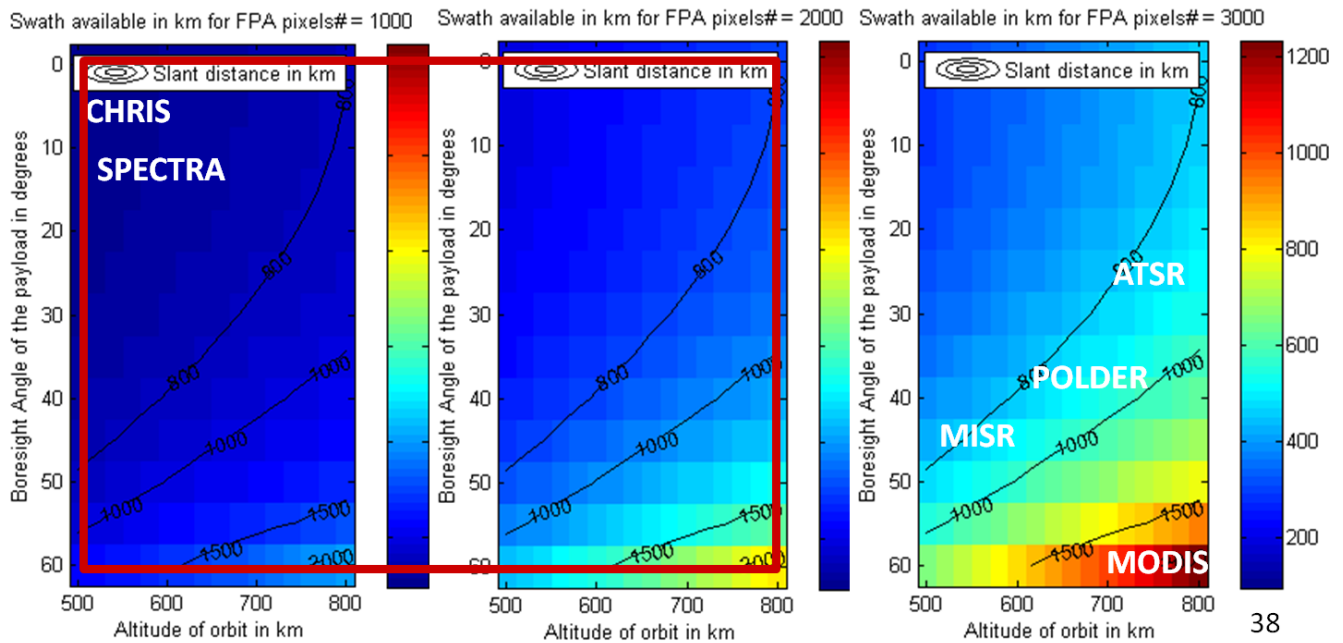


Figure 12: Dependence of swath on boresight angle of measurement, altitude of the satellite and the number of pixels available on the FPA. The ideal swath is on the bottom right corner of the rightmost panel. Current BRDF missions have been labeled in white and the BRDF mission concept delineated by a red box on the tradespace.

Assuming pushbroom sensors as the image acquisition instrument, using the above baseline values for aperture diameter, focal length and pixel sizes, the across-track swath available using these front end optics is shown in Figure 12 for varying number of detector pixels, altitude and boresight angles. The black contours mark slant height corresponding to the altitude-angle pairs. The figure shows where some of the current space missions with

BRDF products (Table 1) lie on the swath tradespace. MODIS has ground pixels that are 250m-1000m in length however has only 10 pixels on its spatial dimension of the FPA. It scans the cross track by $\pm 55^\circ$ to achieve its huge swath. POLDER has ~ 200 km swath but at a very coarse resolution of 6-7km and CHRIS has the same swath at a 25m resolution therefore compensating on its coverage. Currently, the number of pixels is limited within manageable 2000 pixels for at most 2 detector pixels per ground pixel. This corresponds to an FPA length of 2 mm, 3 mm, 6 mm and 8 mm for the 4 proposed wavelength band ranges (for 2000 pixels on all), which is achievable within nanosatellite optics. The area of interest is marked with a red box in Figure 12. Note that the swath is the same for all wavelength bands in spite of each having a different ground pixel size and therefore detector pixel size. The swath will change only if we allocate a different number of pixels or a different FPA size to the different bands.

Whiskbroom scanners are not considered for the BRDF cluster mission because they have mechanisms that increase the risk of failure and have rotating elements that may disturb the attitude control system, which is critical for correct payload pointing. For pushbroom sensors, the “swath” in the along track direction is only one ground pixel (gps) wide. Thus, for the BRDF mission, pushbroom scanners have the disadvantage of being extremely susceptible to attitude control errors in the nadir direction. A nadir pointing error of $\Delta\eta$ results in a mapping error on the ground of $\Delta\eta \cdot D / \sin\epsilon$ where D is the slant distance to the ground and ϵ the elevation angle. This means that even when the payload is pointed vertically downward, an angular error equal to the iFOV will cause the payload’s ground pixel to completely miss overlapping with ground pixels of the other satellites in the cluster. As the nadir pointing angle increases and elevation angle decreases, the mapping error gets worse and at 60° nadir pointing angle, an error of less than a fifth of iFOV causes a complete miss. An azimuthal pointing error of $\Delta\phi$ results in a mapping error on the ground of $\Delta\phi \cdot D \cdot \sin\eta$ where D is the slant distance to the ground and η the nadir pointing angle. However, since the cross track swath is multiple orders higher than the along track swath, probability of entirely missing the overlap is much lower. To overcome the above risks, matrix imaging is a better choice than pushbroom imaging, that is if we have 1000 spatial pixels, it is less riskier to image a 20×50 spatial spot than a 1000×1 spatial vector. However, since matrix spectrometers have never been demonstrated in nanosatellite, the project to design one is going to be challenging.

For a total of 1600 spatial pixels that is the average of the number of pixels in Figure 12, the matrix FPA will contain 40×40 pixels and result in a swath between ~ 4 km to ~ 16 km (variation with altitude and boresight angle). The FPA detector plate will be less than a mm for all the wavelength bands proposed. Assuming the baseline diameter of 7 cm, the power received at the sensor can be calculated by the following equation derived from first principles – conversion of FOV to steradians and multiplying by the angle as well as the aperture surface area:

$$P(\lambda, \eta, h, SZA) = L(\lambda, \eta, SZA) * BW(\lambda) * \left(\pi * Da * \sin\left(\frac{FOV}{4}\right) \right)^2$$

Equation 8

Where FOV = the full field of view achievable using 1600 detector pixels in a 40×40 matrix as calculated similar to Equation 1, Da = aperture diameter, $BW(\lambda)$ is the bandwidth of the wavelength considered and $L(\lambda, \eta, SZA)$ is obtained from the COART model. This power is expected to be further reduced as a function of the optical transmission characteristics of the spectrometer and the quantum efficiency of the detectors. Figure 13 shows the dependence of power on wavelength of radiation and ground resolution. A monotonic decrease is seen in the visible range of light alone over nearly an order while about half an order of magnitude decrease is seen for a full range of change in the solar illumination angle. The power values at 1010 nm are chosen (marked with a white

arrow on the right panel of Figure 13) to demonstrate the variation of power with respect to altitude and boresight angle in Figure 14. The dependence on altitude is negligible compared to angles because COART radiance is barely affected by altitude above 100 km and slant height and therefore FOV varies far more due to look angle than orbit altitude. A variation of power levels from 1.56×10^{-7} W to 2.38×10^{-12} W is estimated for the entire range of design variables considered – ground resolution, λ , SZA, altitude and boresight angles.

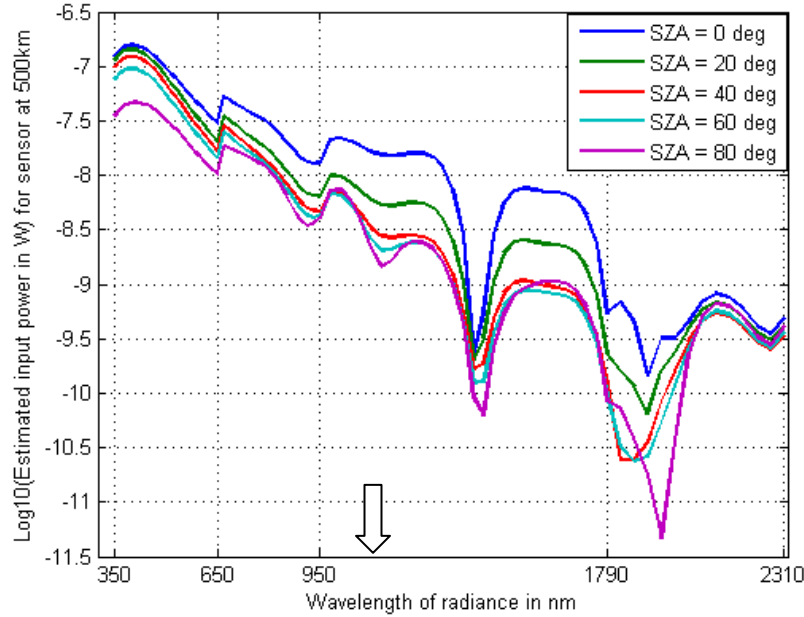


Figure 13: Power received by the optical sensor at slant height = 500km for an aperture diameter of 7 cm using 1600 detector pixels in a 40 X 40 2D spatial matrix and different solar zenith angles, as calculated from the COART model estimates. The bands delineated on the X Axis correspond the 4 potential bands in the proposed spectrometer.

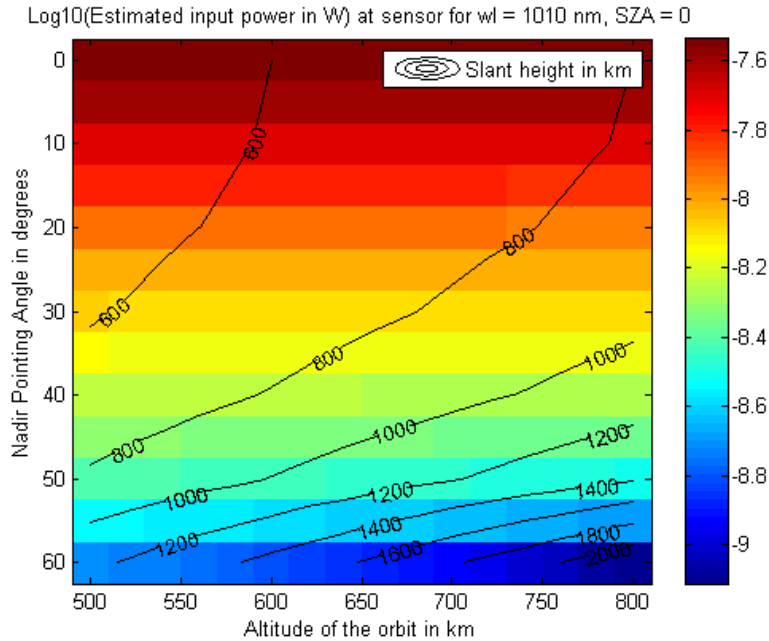


Figure 14: Power received at the LEO sensor as estimated from the COART model for a specific wavelength picked from Figure 13 (marked with a white arrow) for varying altitude and nadir viewing angles. The slant distances, a function of angles and altitude, have been contoured.

Given the typical ground velocity of ~7.6 km/s of each spacecraft, the requirement to continuously sample along track and the minimum swath available of 4 km (from previous calculations), the maximum integration time available is $4/7.5 \sim 0.5$ seconds. The variation of energy levels will thus be $7.8\text{e-}8$ J to $1.2\text{e-}12$ J which is approximately a range of $1\text{e}6$ to $1\text{e}11$ photons – five orders of magnitude. However, since the spectrum is divided into 4 ranges, the variation is only an order for the first two ranges and two orders for the last two ranges. The radiometric range of the detectors should be sensitive to this variation within the spectral range.

Optical transmission and thus final detectable power will depend on the specific spectrometer selected; will be discussed in Section 3. The signal to noise ratio (SNR) will depend on the detectors selected. For CCD detectors, it is given by the CCD equation [35] - Equation 9 – where N_* is the total number of signal photons (requirement 9 in the previous section). The major contributors of noise are readout noise (N_R = photons generated when no light shines on the detectors), dark current noise (photoelectric effect electrons generated by the heat produced by the system or thermal noise that cannot be distinguished from electrons generated by photons) and random sky noise (photons from background or sky). All the noise factors, other than sky noise which is a function of environment, depends on the detector array and scales linearly with the number of pixels imaged.

$$\frac{S}{N} = \frac{N_*}{\sqrt{N_* + n_{\text{pix}}(N_S + N_D + N_R^2)}}$$

Equation 9

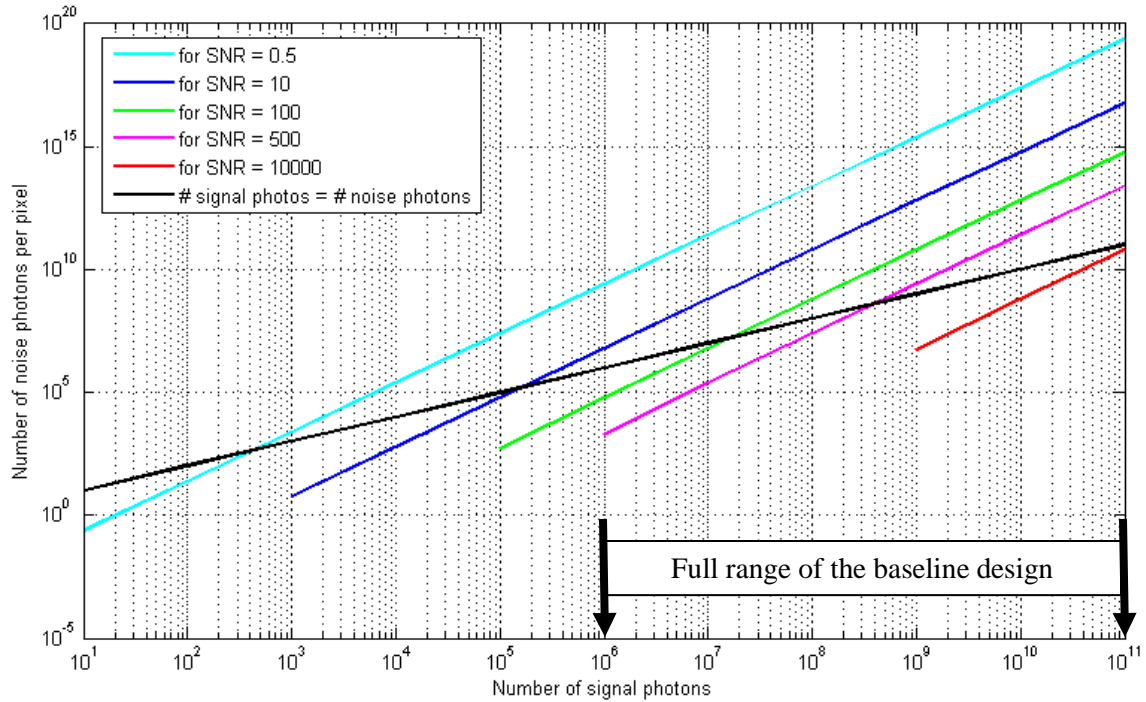


Figure 15: Relationship between number of signal and noise photons for a given SNR by Equation 9

SNR represents a very nonlinear relationship between the number of signal and noise photons as seen in Figure 15. All designs above the black line indicate that the number of noise photons per pixel is greater than the signal available from the object of interest. For a given number of signal photons, the SNR for which the noise photons are less than signal photons can be calculated. This required SNR increases tremendously with increasing signal

photons that is the size of the extended object being imaged and the wavelength at which it is imaged. For $1e11$ photons, which is the expected maximum for the baseline design's 4th wavelength range, the required SNR is 10,000 (pink curve in Figure 15) – a huge value compared to an SNR of 200 for the airborne AVIRIS instrument [19] or of 250 for CHRIS [36]. The required SNR for the first wavelength range similarly is 100.

Practically though, the number of signal photons is lower than the values quoted because they also depend on sensitivity issues of the CCD detectors which are not able to convert all of the photons that strike the surface into electrons, and so have a lower required SNR. The most important determinants of sensitivity are:

- Quantum efficiency (QE) which is the ratio of incoming photons to those photons actually detected by the CCD and is between 50%-90% in the operational range of the CCD. Detectors with maximum quantum efficiency within the chosen bands should be used
- System gain which represents the number of electrons which cannot be resolved by the Analog to Digital Converter (ADC)'s bits. More the number of bits available, higher the gain.
- Charge transfer efficiency (CTE) which describes the level of accuracy that the charge stored in each pixel can be transferred from one pixel to another in the readout process
- Well depth total amount of charge (number of electrons) that can be stored in the pixels before the charge overflows into adjoining pixels through a process called blooming. It is proportionate to the pixel size

The *functional requirements of the sensor system*, as learned from the trades above, can be summarized as:

1. Four wavelength band ranges, as split by dichroics and fed into different dispersive elements, with resolutions of 30, 15, 28 and 30 respectively
2. Focal length of 10-11 cm to be able to achieve the required ground resolutions and boresight view angles
3. Aperture diameter of 7 cm for an F# of 1.5 for diffraction limited imaging for up to the longest wavelength
4. Pixel size of 1 μm , 1.5 μm , 3 μm and 4 μm for the proposed wavelength bands
5. At least 1600 pixels on the detector array, preferably in a 40 X 40 matrix for 2D spatial imaging
6. SNR of between 100 and 10000 to account for noise photons, depending on the wavelength range. Exact SNR calculations will depend on the spectrometer and detectors chosen
7. 16 bit detector pixels to capture the radiometric variations calculated per wavelength range in the trades
8. Detectors with well depths to accommodate greater than $1e6$ to $1e7$, $1e7$ to $1e8$, $1e8$ to $1e10$, $1e9$ to $1e11$ in the four wavelength band ranges respectively. Specifications of typical CCD arrays and InGaAs diodes show that both this requirement and the previous one is possible to achieve in nanosatellites
9. Detectors with minimum detectable photon levels greater than the number of noise photons generated in the detector

As demonstrated though trading for optical parameters and selecting a baseline, the goal is to design a system that will meet the BRDF requirements optimally, generate hundreds of architectures by varying the technical parameters and requirements within the allowed constraints and technological feasibility followed by a trade between the technical performance and the cost/mass/complexity of the system to converge on a final design.

3. Instrument Selection and Design

A generalized spectrometer with its basic components is shown in Figure 16.

The high level optics parameters and their dependencies on mission requirements such as cluster geometry have been modeled in the previous sections and some baseline values identified through tradespace analysis. While

most instrument parameters will be calculated using these values for demonstration purposes, selection of the instrument will require consideration of all the architectures.

CCD arrays will be used as detectors. As mentioned before, the incoming light will be split into 4 paths using dichroics before it is incident on the dispersive element and imaged on the detector so that different detector elements can be used for different parts of the spectrum that it is most sensitive at. For example, silicon detectors work best between 350 nm to 1000 nm while InGa, InAr or GaAs detectors work best for the NIR to short wave IR range of 1000 nm – 2500 nm [34]. InGaAs is picked as the detector of choice because it has high D^* (detectivity), low dark current, and responds to the whole SWIR range for modest cooling (150K-200K as demonstrated in ESA's SCIAMACHY instrument [37]) so that a major portion of the instrument's mass and power budget is not consumed by the focal plane cooler. COTS FPAs of up to 1260 X 1260 pixels with a 20 μm to 30 μm based on InGaAs detectors with spectral resolution up to wavelengths of 2.6 μm have been documented in literature [38]. For the baseline design of 400 X 400 pixels calculated in the previous section, these detectors are a great match.

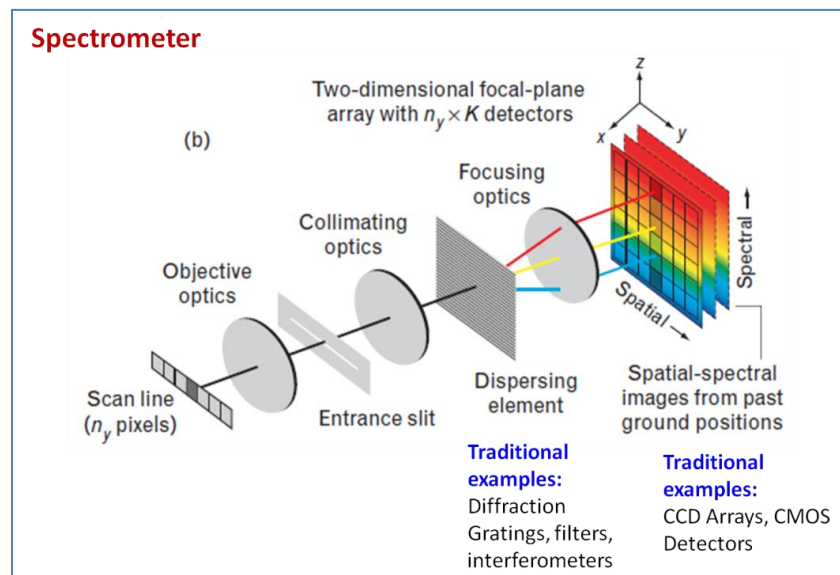


Figure 16: Generalized spectrometer adapted from [39]

While the dispersive elements have traditionally been diffraction gratings, filters and interferometers, these are best applicable for imaging a vector of spatial elements multi-spectrally. Gratings cannot be used for matrix imaging because if 2 dimensions are spatial, then the spectral dispersion needs to occur in the third dimension which typical diffraction gratings do not have [33]. Therefore, there is a need to adapt available spectrometer designs other than traditional gratings to perform matrix imaging, that is expand the columns in Figure 16 to a 2D matrix.

There are several miniaturized spectrometer designs which have been demonstrated in theory and flight. These include MEMS based grating spectrometers [40], MEMS based interferometric spectrometers (Fabry Perot [40], [41] as well as FTS with moving gratings [42]), spatial heterodyne spectrometers using regular gratings [43] and double grating slab spectrometers [44]. One of the simplest designs for pushbroom multispectral imaging is to put the bandpass filters on the detector array as horizontal rows in Figure 16, instead of on the first pupil, to allow different spatial pixels of specific bands to reach the detector. This design offers the advantage of eliminating all dispersive and optical elements and therefore spectral aberrations, as well as restricts the entry of stray light

anywhere in the system. Unfortunately, none of the above designs are adaptable to 3D imaging (2D for spatial and 1D for spectral). Literature search revealed three possible designs which can be used for earth remote sensing of extended objects and their applicability to the BRDF nanosatellite clusters has been discussed below.

3.1. Waveguide Spectrometers

While in bulk optics, Fourier-transform (FT) spectrometers offer throughput advantages compared to dispersion devices, they typically involve mechanical scanning of the optical path in a Michelson interferometer. Spatial heterodyne spectrometry (SHS) is a static Fourier technique based on spatially distributed interferograms formed by diffraction gratings that replace the Michelson mirrors or use mirrors that are introduced in a waveguide channels. Waveguide Spectrometers have popularized in the last few years as the “Spectrometer on a Chip” where the idea is to use multiple waveguides of varying lengths to introduce a path delay in different arms of the incident beam of light. The waveguides are photonics light-wave circuit (PLC) waveguides used as the basis of its interference phenomenon [45]. Advantages of PLC waveguides include miniaturization of spectrometers, no moving parts, no internal vibrations, low power, shock resistant and easily radiation-hardened [46]. Each detector pixel needs a chip which has a single optic to focus light from a broad FOV to the integral chip and this into an array of waveguides of varying length [47] that induce phase differences, causing the interference.

The waveguide spectrometers can be of 2 types:

1. *FTS (Fourier Transform Spectrometer) type in the traditional Mach Zehnder or Michelson Interferometer configuration* which uses mirrors within the waveguides on the PLC. The original spectrum is split into several pairs of beams and each pair delayed in phase using waveguides of varying length (Figure 17). The pairs are then made to interfere at the detector and due to the differing optical path delays between the pairs, the interferogram at the detector forms a Fourier transform pair with the original spectrum. A Fourier transform of the same returns the original spectrum [48].

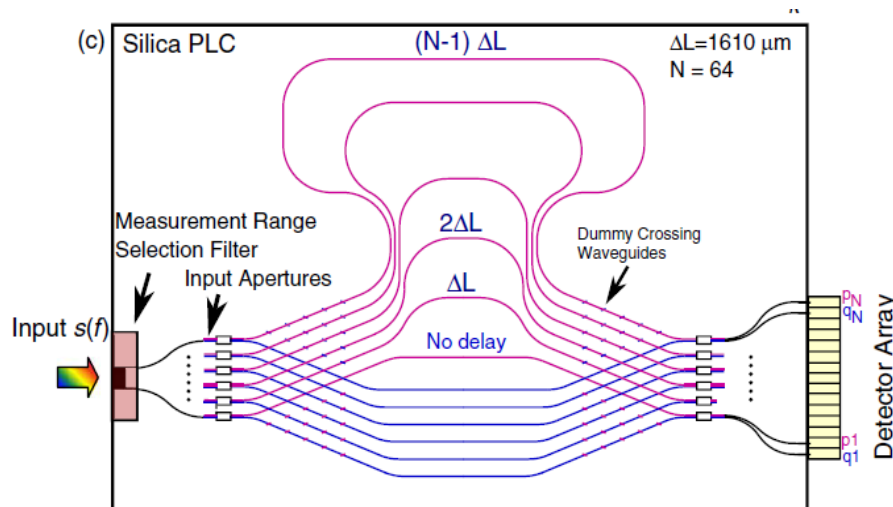


Figure 17: Paths inside a Fourier-transform, integrated optic spatial heterodyne spectrometer on a Si-based waveguide. Light enters the waveguides on the left and produces an interferogram on the detector array on the right. Fourier transform of the interferogram gives the original spectral distribution.

Equation 10 shows that the relationship between the input and output power of in the waveguide FTS is a discrete cosine transform, as verified empirically in [48], where $\bar{\sigma}$ is the difference between the central wavenumber and the highest wavenumber being imaged, N is the number of waveguide strands, Δx is the maximum optical path delay desired (function of propagation efficiency and waveguide length) and x_i is the spatial coordinate on the output FPA.

$$P^{in}(\bar{\sigma}) = \frac{\Delta x}{N} P^{in} + 2 \frac{\Delta x}{N} \sum_{i=1}^N W(x_i) F(x_i) \cos 2\pi \bar{\sigma} x_i$$

Equation 10

Calibration errors can also be calculated from the inverse relation of Equation 10 using linear regression applied to inteferogram points for a matrix of path delays.

2. *Grating type based on PLC arrayed waveguides* which uses a grating within the waveguides to form Fresnel [49] or Fraunhofer [50] diffraction fringes. The interferogram at the image plane is caused due to multi-beam interference of the diffracted beams with an optical path delay due to different waveguide lengths. Monochromatic light produces sinusoidal fringes of period $d(\lambda)$ while an arbitrary input spectral density $B(\lambda)$ will produce an interference pattern $I(x)$ where x is the position along the interference pattern as given in .

$$I(x) = \int_0^\infty B(\lambda) \left[1 + \cos \frac{2\pi}{d(\lambda)} x \right] d\lambda.$$

Equation 11

In traditional grating spectrometers, wavelength resolution can be improved by reducing the slit width leading to a reduction in optical throughput. The interference approach using gratings does away with the relation between input slit and resolution and thus allows more throughput per resolution than traditional gratings [51]. An Arrayed Waveguide Grating (AWG) can be made using gratings in waveguides and the waveguide SHS spectrometer can be formed by interleaving two AWGs having opposite dispersion. The interleaved arrays produce two wavefronts that propagate and mutually interfere in the slab waveguide yielding wavelength-dependent fringes. This is due to the different dispersion of the arrays which makes the wavefronts intersect at different angles for different wavelengths thus forming wavelength-dependent fringe patterns as shown in Figure 18. In general the input spectrum is related to the fringe pattern via Fourier transform since any input signal can be decomposed into its monochromatic constituents. This interleaved AWG arrangement allows using a wider input waveguide width compared to a standard AWG of similar spectral performance.

The FTS type has important advantages over the grating type – they have large optical throughput for the same spectral resolution because of the lower probability and intensity of ‘crosstalk’ between the different waveguides [52], ability to calibrate theoretically for ideal path delay and through simulations for non-ideal delay [48] and ability to correct interferometric defects in the post processing phase [47]. The main performance criteria are spectral range and resolution, optical crosstalk, optical loss and polarization wavelength dependence. NASA GSFC is currently developing the waveguide FTS for multi-angular radiance measurements as shown in Figure 19 and has demonstrated improved performance using the compact design on the right panel.

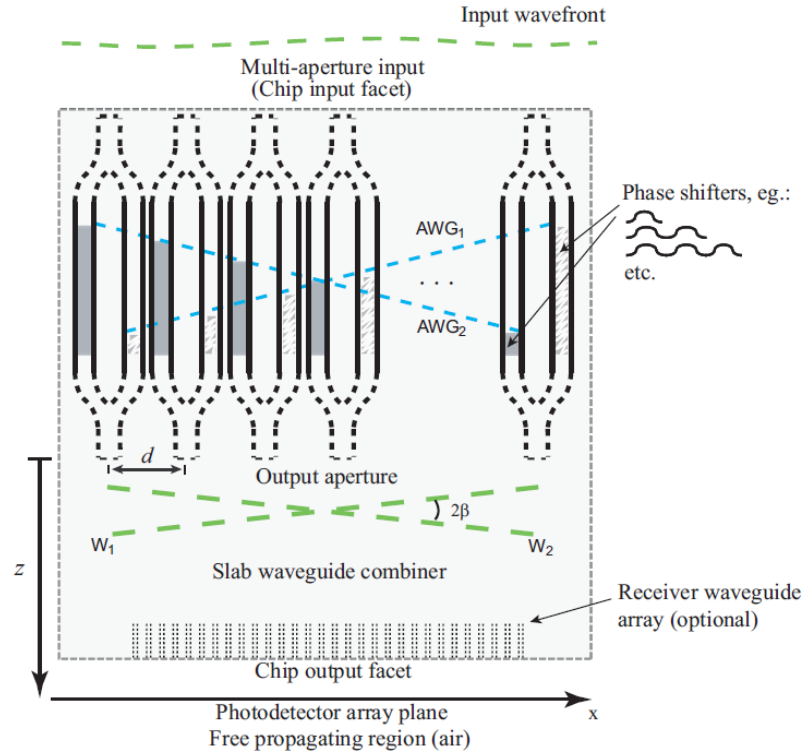


Figure 18: General schematics of a FT AWG microspectrometer with two interleaved Arrayed Waveguides (AWGs) as published in [49]

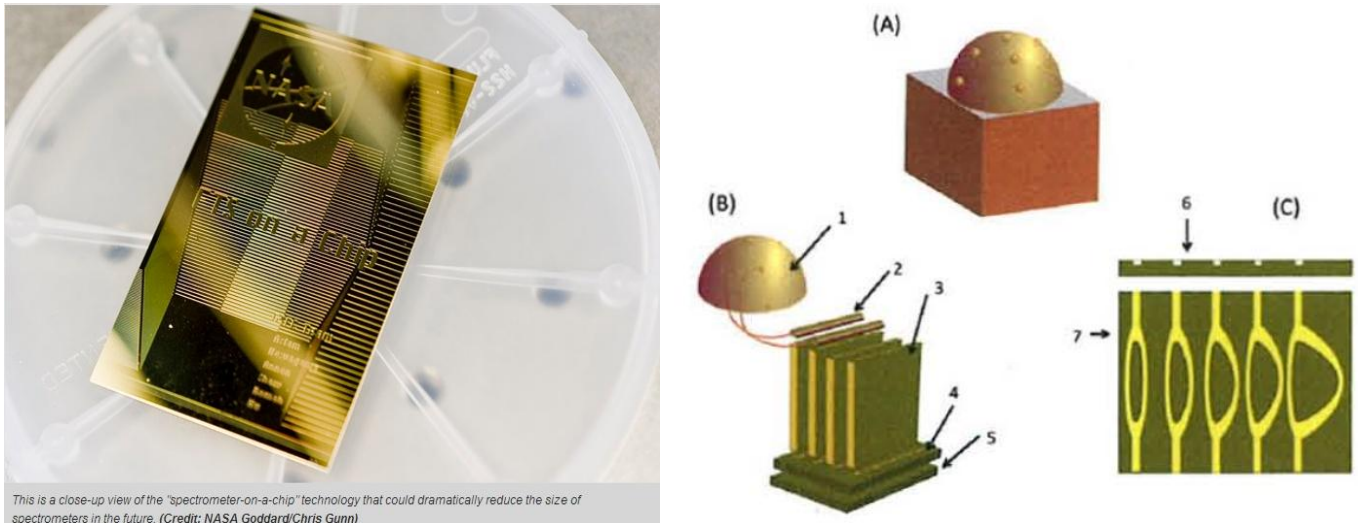


Figure 19: The Spectrometer on a Chip concept developed by NASA GSFC for mid IR wavelengths [46]. The left panel shows the Addressable Photonics Cube (APC). The right panel shows a schematic view of the APC in (A) and its components in (B). The components include a dome with apertures to let light in from different directions – 1, fibre-optic couplers – 2, Spectrometer on a Chip modules – 3, 2D detector array – 4, FPGA – 5. (C) shows the Spectrometer on a Chip components – the waveguides.

Based on the fact that the length of the waveguides vary linearly from 0 to L_{\max} , which is a function of resolution, central wavenumber and efficiency, the number of waveguides needed [51] is given by Equation 12 where $\Delta\lambda$ is the spectral range of the spectrometer, $\delta\lambda$ is the spectral resolution and R is the resolution of the dispersive element as defined in Equation 6.

$$N = 2 \frac{\Delta\lambda}{\delta\lambda} = R$$

Equation 12

This means that for a spectral ranges of Figure 7, the total number of waveguides needed will be $2 * 85 = 170$ – which has been demonstrated in the laboratory and published in literature [52], [51]. For a 6 μm pitch of the waveguides [51], the chip breadth will be ~ 12 mm (6 μm pitch times 200 waveguides). The length of the chip needed would be given by L_{max} in Equation 13 [51] where R is the resolution, k_0 is the wavenumber at Littrow wavelength and n_{eff} is the mode effective index. For the wavelength resolutions and central wavelengths proposed in our spectrometer's 4 band ranges, the corresponding L_{max} for the ranges are 18.75 mm, 15 mm, 47.95 mm and 33.3 mm. Thus, the length of the chip for the 4 wavelength ranges should be atleast L_{max} .

$$L_{\text{max}} = \frac{R}{k_0} \frac{2\pi}{n_{\text{eff}}}$$

Equation 13

The thickness of the chip is the length of a waveguide and the glass required to etch it (cradle size), less than a 1 mm. Each chip is therefore estimated to be ~ 12 mm X [18.75 mm, 15 mm, 47.95 mm, 33.3 mm] X 1 mm. For 1600 spatial pixels, 1600 chips will be needed which will occupy a volume of less than 10 cubic cm or the size of one cube in a Cubesat. This compact volume is possible because the Mach Zehnder waveguide strands can be interleaved to reduce the collective volume by 2-3 times compared to the simple stacked layout [52]. If a separate dispersive unit is needed for each wavelength range, then 4 such cubes will be required, causing this design to be a pretty large by nanosatellite standards. The electronics associated with the operations weigh less than 0.7 kg and the chips are less than a milligram, easily achievable within nanosatellite mass constraints. This design can be used for matrix imaging because each spatial pixel has its own chip, thus the arrangement of the pixels as a vector or matrix is not important.

While FT spectrometers without moving parts (spatial heterodyne spectrometer) have been developed and flight-tested for UV (SHIMMER [53] launched in 2007) and IR wavelengths (SHOW [54] not launched yet), the development of the same on PLCs is less than 5 years old. Its TRL is estimated to be between 5 and 6. One of the biggest constraints in the development cycle is to develop methods to eliminate crosstalk between adjacent waveguides which is estimated to increase with decreasing bandwidth [51].

3.2. Acousto-Optic Tunable Filter Spectrometers

Acousto-optic tunable filters (AOTF) offer a mechanism to filter broadband incident light by achieving the spectral decomposition in time due to its high spectral agility, and therefore allows spatial matrix imaging. An AOTF device [55]–[57] can switch from one spectral range to another in the time that it takes an acoustic wave to traverse a solid state crystal (typically tens of microseconds). An acousto-optic cell – marked in green in Figure 20 and in the top panel to the left of the CCD detector in Figure 21 – is a transparent birefringent crystal excited by a radio frequency transducer. Acoustic waves propagate inside the crystal and create regular spatial variations of the refractive index. Under phase-matching conditions, light of a particular linear polarization and wavelength, incident on the crystal at a very specific angle, is diffracted by the moving grating produced by the acoustic wave. The conditions favoring diffraction are only satisfied for a particular spectral frequency at a particular incident angle and a particular driving frequency so by controlling the transducer frequency, the spectral frequency

diffracted can be selected. Controlling the transducer power allows control of the amount of light diffracted. Typical transducer power is on the order of 1 W. While higher transducer power increases the amount of diffracted light, it also degrades spectral resolution by increasing sidelobes of the center frequency. Although a number of birefringent materials have been used for AOTF devices, TeO_2 is a frequent choice due to its high acousto-optic figure of merit, and good transmission in the visible and infrared, (350 nm -5000 nm). Other materials include TAS, which is transparent to 11 μm , and quartz which is transparent in the UV.

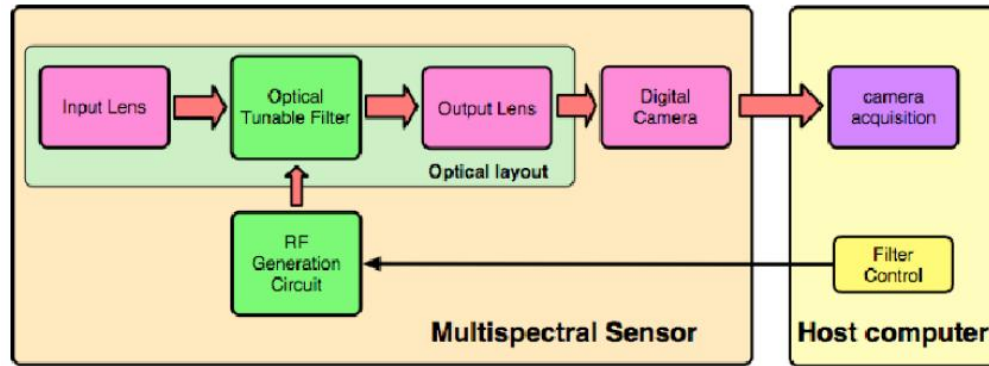


Figure 20:Block diagram of the AOTF cell and its interfaces with the front end optics and back end avionics [58]

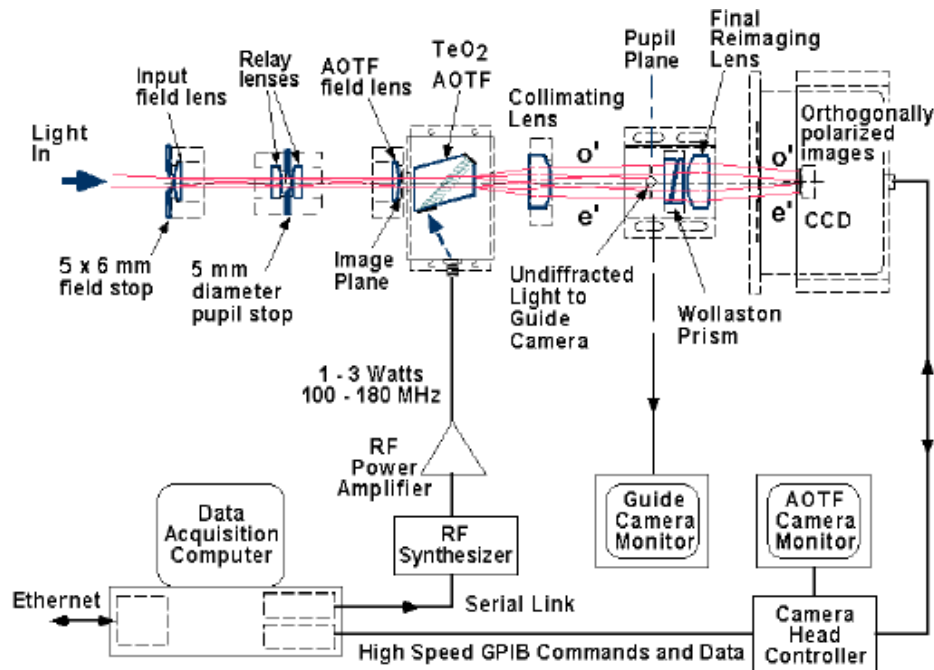


Figure 21: Detailed AOTF system as published in [57]

AOTFs can be used for multispectral matrix imaging because the AOTF can be tuned to the first desired band, the 2D spatial matrix imaged at that band, signal integrated over the integration time period, CCD read out and the process repeated for the next wavelength band until all 85 bands are exhausted. The tuning time is only a few microseconds thus the rate determining step in the process is the CCD readout time. At a typical rate of 1 megapixel per second, the time taken to read 1600 pixels is 1.6×10^{-3} seconds and thus the total imaging sequence

per 2D spatial image will take at least $1.6\text{e-}3 * 85 = 0.1365$ seconds. As calculated in Section 2, the maximum time available between sequential images is ~ 0.5 seconds. The AOTF tuning process takes away nearly 30% of the time that is usually available for signal integration and, thus, reduces the effective signal to noise ratio. The advantage, on the other hand, is that only two dispersive elements are needed for the entire spectral range because the ranges will only depend on the detectors used at the end of the AOTF cell – Silicon or InGaAs. This is in contrast to waveguides where the range has to be divided into 4 sub ranges to also account for the free spectral range.

The AOTF spectrometer has two units – Optical which consists of foreoptics, AOTF crystal, imaging optics and the camera as seen in Figure 21. The Electronic unit controls the AOTF, Camera, power supply, etc. The weight of the optical unit is in the ballpark of 1 – 1.2kg, the electronics within 0.5 kg to 0.7 kg which brings the total spectrometer mass to within 4-5 kg [59]. AOTFs have significant heritage since they were used recently on the Mars Express [60], the Venus Express [61] and also to probe Titan’s atmosphere back in 1999 [62]. The TRL of this spectrometer design can thus be estimated at 8-9.

3.3. Integral Field Spectrograph

An integral field spectrograph (IFS) is a 3-D-type device that can gather spectra at every spatial element in its field of view. Although IFS-type instruments are used in ground-based observatories, including the Keck Observatory in Hawaii, the technology has been demonstrated in spaceflight just once [63] and is currently being used in the development of the CHARIS instrument to look for exoplanets on small satellites.

An IFS simultaneously obtains spatial and spectral information over the field of view by dispersing the entire image on the detector using lenslets to sample the image plane [64]. Each lenslet samples a piece of the image and focuses it to a point spread function (PSF). Each PSF is dispersed and then imaged by the multiple detector elements as seen in Figure 22. This allows the IFS to measure two spatial and one spectral dimension simultaneously by mapping all 3 dimensions onto the 2D detector plane by spreading the spectrum over multiple spatial pixels. IFS offers the advantage of low mass and volume as well as a medium TRL (6-7) for the technology and low TRL (5-6) for the same in small satellites. The disadvantage is that each dispersed spectrum for a spatial pixel may take up to 35 detector pixels in length and 6 pixels in width (focused by a lenslet element)[64] causing a significant reduction in the number of pixels available for spatial imaging. Also, processing required to deconvolve the spectral and spatial data from the same detector array may be complicated.

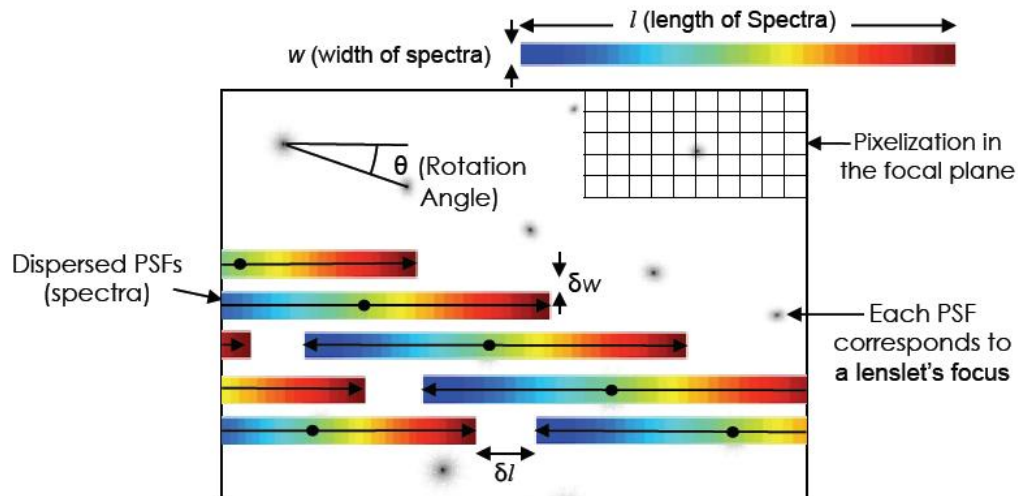


Figure 22: The layout of the spectra and pre-dispersed PSFs on the detector of an IFS as published for the CHARIS instrument [64]

3.4. Mapping of Functional Requirements to Instrument Form

The three proposed instruments (forms) are demonstrably capable of achieving the dispersive and spectral functional requirements of matrix spatial imaging as shown in the previous sections. The instruments are now summarized in Table 4 in terms of their relative fit within nanosatellite resource constraints and the relative performance with respect to standard spectrometer parameters. All three can fit within the mass, volume and power requirements of small satellites, so are low compared to traditional designs – the table shows their relative rank among each other.

Spectrometer Types:	Waveguide Spectrometers [52]	Acousto-Optic Tuning Filters [56]	Integral Field Spectrograph [64]
System Resource Metrics:			
Mass	Medium	Low	High
Volume	High	Medium	Medium
Power	Low	High	Low
TRL	Low	High	Medium
System Performance Metrics:			
Required Num of pixels	Medium	Low	High
Susceptible to aberrations	Medium	Low	High
Resolution per aperture	High	Low	High
Optical Throughput	High	Medium	High
Polarization Measurement	Medium	High	Low
Spectral Range	High	Low	Medium

Table 4: Comparison of the selected matrix imaging spectrometers in terms of resource and performance metrics. The colors indicate whether the parameter evaluation is good (green), acceptable (yellow) or bad (red) compared to the other 2 instruments considered.

The system performance metrics evaluated are:

- *Required number of pixels to achieve the same spatial and spectral coverage and resolution:* IFS samples 3D onto a 2D array thus needs an order of magnitude more pixels. AOTFs sample the spectral dimension in time and therefore do away with the requirement of more pixels and varied dispersive elements to account for sub-ranges
- *Susceptibility to spatial and spectral aberrations:* Waveguides spectrometers rely on the fourier transform of the spectrum, aberrations can be compensated for mathematically [48]). IFS runs the risk of overlap of the spatial and spectral components if the lenslet focuses erroneously hence leads to higher aberrations if not deconvolved correctly.
- *Achievable resolution for the same aperture diameter:* AOTFs have been demonstrated in space with a field stop of 1-2 cm for the AO cell however the cell can be connected to a large aperture telescope (>2 m used for imaging Titan [62]) however, the more the ratio of apertures, the more the required focusing optics or alternatively, the less the light intensity available through the AO cell.
- *Optical throughput of the full system:* It is very high for waveguide spectrometers with well prevented crosstalk, even compared to large traditional spectrometers, because they use total internal reflection with minimal loss of energy between the filters and the FPA
- *Possibility of measuring the Stokes' vector or polarization state from the incident light:* Since AOTFs use the birefringent crystals, the index of refraction of the "ordinary" axis differs from that of the "extraordinary" axis. By imaging 2 diffraction orders (-1 and +1), it is possible to calculate polarization with some addition to system size. IFS also has the possibility to expand to include polarization [65] capabilities but for a much higher addition of pixel numbers than waveguides.
- *Possible spectral range within the BRDF spectrum of interest:* AOTF crystals are made of TeO_2 which, for practical applications, is transparent above 350 nm. The CAR airborne instrument has a band of interest at 330 nm which cannot be sampled using AOTFs unless a bandpass filter is applied for the UV range and quartz is used as the crystal, which in turn requires more transducer power. Waveguides have much more flexibility in spectral range as do IFS, but for a much higher number of pixels.

One specific design out of the above three has not been selected because all seem to be within acceptable performance as per preliminary analysis. Their evaluation metrics can be used to in the system level trades of the whole cluster system later, to select the one best for a particular architecture.

4. System Testing

Calibration of the spectrometer will be required both pre-flight in the laboratory and also periodically in-flight. Before launch, the different components of the spectrometer need to be unit tested followed by testing after being integrated into the full system to check for unwanted emergent behaviors. The calibration and test plans will be described briefly below

4.1. Calibration Methods

Pre-flight calibration is best achieved using integrating spheres available within Goddard's airborne BRDF test facility [66]. The instruments used to calibrate include three integrating sphere sources (ISSs) operated at different light levels and experimental setups to determine radiance variability. The radiance gradients across the three ISS apertures were 0.2%–2.6% for different visible, near infrared and shortwave infrared illumination levels but 15%

in the UV. Integrating spheres for laboratory calibration are now very well accepted and have been used in AVHRR, MODIS and MISR.

Integrating spheres can be used for three types of tests:

1. Three integrating sphere sources (ISSs) are made to shine at different light levels as determined by the number of operating lamps—from 0–16 available lamps to ascertain linearity over the instrument performance range and to convert instrument digital counts into radiance units.
2. Measurement of the responsivity of the spectrometer (defined here as detector output per unit of incident power at a particular wavelength) at more than nine different distances from the ISS aperture to ascertain the sensitivity of calibration to distance of separation between the spectrometer and the ISSs
3. Determining the spectrometer responsivity across the mission angular range of 0 through 60°

The test data above is also used to determine [67] the dark noise of the spectrometer, the frame transfer offset (if an electric shutter is used and additional signals are accumulated when the frame is being transferred), saturation levels of the spectrometer and SNR and the spatial response uniformity of the signal over the detector pixels to show if the pixels have differential optical blur, spatial variation in optical element transmittance and pixel-to-pixel sensitivity differences.

In-flight calibration is more challenging especially in a small satellite with mass and power constraints. Calibration lamps were looked into in spite of their power requirement of <1W but were eliminated on the grounds of strict thermal requirements to keep the filament at a particular temperature. Additionally, the Hyperion spectrometer [68] demonstrated little dependence on lamp based calibration because of long-term instability (as large as 30% increase in the lamp's output) in spite of having an order of magnitude of more mass and power than small satellites. Acceptable calibration methods and their heritage include:

1. Calibration using white diffuser plates to reflect sunlight to the spectrometer as in VIIRS [69] and SELENE [70]. This will need precise knowledge of position and orientation with respect to the sun, a very stable internal diffuser and a mechanism (typically doors are used) to expose the spectrometer to the diffuser's signal instead of the earth and the need to calibrate during the day time. Spectralon [71]–[74] of the space-grade is found to be the best diffuser material because of its very high diffuse reflectance and Lambertian behavior.
2. Lunar calibration by staring at the moon as in the SEVO payload in the O/OREOS spacecraft [75]. This requires precise phase and reflectance knowledge of the moon (the USGS RObotic Lunar Observatory (ROLO) database provides reliable numbers), can be conducted only at night and efficient calibration can be done only twice a month. The moon is a much better candidate to stare at than the sun because the radiometric range of the sun is so large compared to the reflectance values the spectrometer is trying to measure that it will saturate the instrument
3. Vicarious calibration using ground control points of very well known radiance at the BRDF angles and wavelengths such as the New Mexico or the Sahara desert. This can be done in the day and/or night, as shown in the LandSat missions

In-flight calibration checks the same quantities as laboratory calibration methods – responsivity, performance range, linearity, SNR, dark noise and spatial response uniformity. Depending on the attitude control capabilities of the nanosatellites, infrequent but periodic calibration maneuvers may also be planned [69]. These include rolls of different angles to acquire different images of the moon at different phases to track instrument radiometric degradation in the visible, near infrared, and shortwave infrared bands, yaw maneuvers over an angular range to

perform a seasonal mapping of the radiometric performance of the on-board solar diffuser and a full pitch maneuver when the satellite is on the dark side to enable multiple scans of deep space to characterize non-solar infrared response.

4.2. Test Plan

The test plan timeline for the spectrometer is as follows: conduct preliminary feasibility studies of the available spectrometer types and designs that suit the mission requirements, generate a tradespace of technically feasible architectures plotting technical performance vs. cost and complexity, pick a preferred design among these and mature it as a concept baseline. The guidelines set by NASA JPL for the Concept Maturity Levels [76] will be followed through the timeline. CML is a metric like the Technology Readiness Level (TRL) scale for new concept development before the traditional NASA Systems Engineering Cycle begins with pre-Phase A. The concept baseline will then be developed in detailed simulations, potentially can be tested on a high-altitude balloon test through an MIT undergraduate class² or an aircraft flight experiment (for example, in conjunction with the CAR in its next flight), can be calibrated in the NASA Goddard Space Flight Center's (GSFC's) Radiometric Calibration Facility (RCF) before testing it in orbit. Most of the above tests depend on the availability of enough interest in the scientific community to fund the efforts, however, initial feasibility studies and simulations, regardless of the above funding.

Unit tests will be required to check-out the instrument and they include:

1. Vibration Testing: To reduce the risk of failure of the optical alignment of the spectrometer. The system should be subjected to sine bursts and white noise signature tests and the acceleration spectral density measured to compare with nominal values
2. Thermal Testing: To reduce the risk of detector failure due to not maintaining a low enough temperature (CCD and InGaAs needs between 150 K – 200 K [37]) by use of thermal vacuum chamber testing tuned to ambient, cold and hot vacuum conditions. Also, to test the change in optical properties of the spectrometer due to large variation in temperature
3. Software Testing: To verify that the code components work by unit testing and that they interface correctly with the hardware
4. Camera Testing: To verify that the camera meets the requirements
5. Electromagnetic Interference (EMI): Since the ADCS system of the satellites are expected to be reaction wheels with magnetic torquers to dump the wheel momentum and prevent saturation, it is important to determine that both the magnetometers/torquers and the spectrometer can operate without interference from each other
6. Power cycling test: To verify that the energy and power systems are generating power as required and storing enough in the batteries to achieve night-time calibrations, if needed
7. Data Transfer testing: To verify that the back end computer is reading out from the CCD array as expected and storing the data
8. Environmental Exposure tests: To verify that the spectrometer assembly works even after bombardment from protons, intense UV and static charge buildup.

² From an informal conversation with Prof. Olivier de Weck, an instructor for Unified Engineering in Fall 2012

5. Risk Assessment

The risks associated with the instrument are at two levels: instrument level risk and system/mission level risks. They are listed in Table 5 and Table 6.

Risk #	Instrument level risks	Mitigation Strategy
IL1	Presence of uncorrected spatial or spectral aberrations in the optical system (since the case in point is an imaging spectrometer, there is a trade between the spatial and spectral domains)	<ul style="list-style-type: none"> Optical testing of the instrument, choose an instrument where aberrations are lower e.g. waveguide FTS
IL2	Focusing errors of the optics due to structural movements in space (for example, different wavelengths after dispersion do not converge at the same FPA distance)	<ul style="list-style-type: none"> Vibration, thermal and environmental exposure tests Use processing corrections after data acquisition
IL3	Structural failures like the door mechanism for the diffused plate calibration not opening in orbit	<ul style="list-style-type: none"> Vibration, thermal and environmental exposure tests Use multiple in-flight calibration strategies to increase redundancy
IL4	Thermal failures like the detectors not being cold enough to make precise measurements	<ul style="list-style-type: none"> Add redundancy to the thermal control system by using radiators and MLI Consider using active cooling as an absolute back-up such as thermo-electric coolers (<1kg, <5W) [77]

Table 5: Risks associated with spectrometer functioning and ways to mitigate them

Risk #	System level risks	Mitigation Strategy
SL1	Degradation of the communication system: This mission is estimated to generate a large amount of data. From the tradespaces in Section 3, assuming 85 spectral bands, 1600 spatial pixels and 16 bits per pixel (thus 2^{16} levels of data available), gives 2.176 MB/image. Since swath was calculated to be between 4 -16 km, a 10 km average is assumed which means 4000 images per orbit. Each satellite thus captures 8.72 GB of image data per orbit. Availability of 1 ground station with ~ 10 minutes downlink time will need 14.5 MBps data rate per overpass in order to get all the data to Earth. COTS transmitters (e.g. Surrey) can push their typical boundaries and achieve these rates within <5W power but degradation of the same will lead to significant loss of data	<ul style="list-style-type: none"> EMI, structural and software tests Use higher data rate options (more than typical S-Band and QPSK modulation can achieve) to add flexibility of data rate in case of degradation Add multiple ground stations, preferably with large longitudinal separation to distribute the data download
SL2	Interference of downlink data from different satellites in the cluster	<ul style="list-style-type: none"> Use coding protocols to differentiate between data coming from different satellites e.g. GPS EMI testing for satellite cluster to check that the signal do not destructively interfere during download – use a microgravity test facility such as the SPHERES

SL3	Degradation of the power system	<ul style="list-style-type: none"> Power cycling and software tests Add redundancy in functionality which does not use any power to conserve power for those functions that critically require it (payload operations, comm. downlink).
SL4	Degradation of the attitude determination systems: This is specifically important for this mission because precise BRDF, over and above what current single satellites are capable of doing, can only be estimated from measurements of the same ground target at the same time at different angles. Thus, if the ACDS failure causes a satellite/s to point incorrectly and therefore not overlap its ground spot with the others, it leads to the loss of at least one angle of measurement. This failure can scale up to lead to complete loss of the mission requirements even if the spectrometers work perfectly.	<ul style="list-style-type: none"> Use matrix spectrometers to increase the probability of ground spot overlap Conduct system level testing of formation flight control in simulation and in a microgravity test facility such as the SPHERES

Table 6: Risks associated with functional interfaces between the spectrometer and other satellite subsystems and ways to mitigate them

The risks discussed above are plotted on the Risk Matrix (Table 7) as a function of their probability of occurrence and criticality of the consequences if they occur. The more the risk (red boxes), the more important it is to attempt to mitigate the risks right from the planning phase of the mission. The methodology shown in Table 6 and Table 7 will be used to calculate the relative risks and mitigation strategies required for the potential instruments, optical front end and detector parameters against their performance metrics, when selecting a baseline design.

Probability of Occurrence \Uparrow	Consequence Intensity \Rightarrow				
					SL4
					IL4
				IL3	IL1, IL2
			SL3		SL1, SL2

Table 7: Instrument and System risks on the Risk Matrix which evaluates the risks as moderate (green), high (yellow) or extreme (red)

6. Conclusions

This project identifies the need to make radiance measurements of the earth's surface from space at different 3D geometries of solar and sensor viewing in order to estimate the surface's BRDF. The goals are identified after a detailed literature search of spaceborne and airborne instruments to gauge the required science. The science and measurement goals for estimating BRDF are subjected to tradespace analysis to identify the functional requirements of the payload on the satellites constrained within nanosatellite technologies available. The payload

required is a visible and near infrared, matrix imaging spectrometer. Three types of spectrometers capable of matrix imaging are discussed, their parameters to fit with the identified functional requirements calculated and the overall applicability of the instruments to achieve the project goal discussed. Finally, several calibration mechanisms have been listed, a brief test plan delineated, risks identified and possible mitigation measures suggested.

7. List of Acronyms

AIRMISR	Airborne Multi-angle Imaging SpectroRadiometer
ASTER	Advanced Spaceborne Thermal Emission and Reflection Radiometer
ATSR	Along Track Scanning Radiometer
AVHRR	Advanced Very High Resolution Radiometer
AVIRIS	Airborne Visible / Infrared Imaging Spectrometer
CERES	Clouds and Earth's Radiant Energy System
CHRIS/PROBA E/MAS	Compact High Resolution Imaging Spectrometer/Project for On-Board Autonomy MODIS Airborne Simulator
EUMETSAT	European Organisation for the Exploitation of Meteorological Satellites
FAST	Fast Auroral Snapshot Explorer
FPA	Focal Plane Array
FTS	Fourier Transform Spectrometer
GPS	Global Positioning System
GRE	Ground Resolution Element
JPSS	Joint Polar Satellite System
MASTER	MODIS/ASTER Airborne Simulator
MISR	Multi-angle Imaging SpectroRadiometer
MODIS	Moderate Resolution Imaging Spectroradiometer
NPOESS	National Polar-orbiting Operational Environmental Satellite System
PARASOL	Polarization and Anisotropy of Reflectances for Atmospheric science coupled with Observations from a Lidar
PLC	Photonics Light-wave Circuit
POLDER	Polarization and Directionality of the Earth's Reflectances
RSP	Research Scanning Polarimeter
SAMPEX	Solar, Anomalous, and Magnetospheric Particle Explorer
SHS	Spatial Heterodyne Spectrometer
SPECTRA	Surface Processes and Ecosystem Changes Through Response Analysis
SSFR	Solar Spectral Flux Radiometer
SWAS	Submillimeter Wave Astronomy Satellite
SWIR	Short Wave Infrared
TRACE	Transition Region and Coronal Explorer
TRMM	Tropical Rainfall Measurement Mission
VIIRS	Visible Infrared Imaging Radiometer Suite
VNIR	Visible and Near Infrared
WIRE	Wide-Field Infrared Explorer

8. References

- [1] C. K. Gatebe, "Airborne spectral measurements of surface-atmosphere anisotropy for several surfaces and ecosystems over southern Africa," *Journal of Geophysical Research*, vol. 108, no. D13, 2003.

- [2] G. Schaepman-Strub, M. E. Schaepman, T. H. Painter, S. Dangel, and J. V. Martonchik, "Reflectance quantities in optical remote sensing—definitions and case studies," *Remote Sensing of Environment*, vol. 103, no. 1, pp. 27–42, Jul. 2006.
- [3] M. J. Barnsley, A. H. Strahler, K. P. Morris, and J. P. Muller, "Sampling the surface bidirectional reflectance distribution function (BRDF): 1. Evaluation of current and future satellite sensors," *Remote Sensing Reviews*, vol. 8, no. 4, pp. 271–311, 1994.
- [4] J. Esper, S. Neeck, W. Wiscombe, M. Ryschkewitsch, and J. Andary, "Leonardo-BRDF: A New Generation Satellite Constellation," 2000.
- [5] M. O. Román-Colón and A. H. Strahler, "Land observation from geosynchronous earth orbit (LOGEO): Mission concept and preliminary engineering analysis," *Acta Astronautica*, vol. 61, no. 1, pp. 101–114, 2007.
- [6] A. P. Trishchenko, "Concept of a new multiangular satellite mission for improved bidirectional sampling of surface and atmosphere properties," *Earth Observing Systems IX*, pp. 97–108, 2004.
- [7] T. Quaife, M. Barnsley, G. Thackrah, and P. Lewis, "Mission Status of CHRIS/PROBA and its Utility for Sampling the Earth Surface BRDF," *Proc. Remote Sens. and Photogramm. Soc.*, pp. 12–14, 2001.
- [8] X. Xiong, R. Wolfe, W. Barnes, B. Guenther, E. Vermote, N. Saleous, and V. Salomonson, "Terra and Aqua MODIS Design, Radiometry, and Geometry in Support of Land Remote Sensing," *Land Remote Sensing and Global Environmental Change*, pp. 133–164, 2011.
- [9] D. J. Diner, J. C. Beckert, T. H. Reilly, C. J. Bruegge, J. E. Conel, R. A. Kahn, J. V. Martonchik, T. P. Ackerman, R. Davies, S. A. W. Gerstl, and others, "Multi-angle Imaging SpectroRadiometer (MISR) instrument description and experiment overview," *Geoscience and Remote Sensing, IEEE Transactions on*, vol. 36, no. 4, pp. 1072–1087, 1998.
- [10] A. J. F. Prata, R. P. Cechet, I. J. Barton, and D. T. Llewellyn-Jones, "The along track scanning radiometer for ERS-1-scan geometry and data simulation," *Geoscience and Remote Sensing, IEEE Transactions on*, vol. 28, no. 1, pp. 3–13, 1990.
- [11] C. Godsalve, "Bi-directional reflectance sampling by ATSR-2: a combined orbit and scan model," *Remote Sensing*, vol. 16, no. 2, pp. 269–300, 1995.
- [12] U. Del Bello, J. L. Bezy, J. Fuchs, and M. Rast, "System definition of the ESA Earth Explorer SPECTRA mission," in *Proceedings of SPIE*, 2003, vol. 4881, p. 1.
- [13] P. Y. Deschamps, F. M. Bréon, M. Leroy, A. Podaire, A. Bricaud, J. C. Buriez, and G. Seze, "The POLDER mission: Instrument characteristics and scientific objectives," *Geoscience and Remote Sensing, IEEE Transactions on*, vol. 32, no. 3, pp. 598–615, 1994.
- [14] M. J. Barnsley, J. J. Settle, M. A. Cutter, D. R. Lobb, and F. Teston, "The PROBA/CHRIS mission: A low-cost smallsat for hyperspectral multiangle observations of the earth surface and atmosphere," *Geoscience and Remote Sensing, IEEE Transactions on*, vol. 42, no. 7, pp. 1512–1520, 2004.
- [15] M. A. Cutter, "A low cost hyperspectral mission," *Acta Astronautica*, vol. 55, no. 3, pp. 631–636, 2004.
- [16] B. A. Wielicki, B. R. Barkstrom, E. F. Harrison, R. B. Lee, G. L. Smith, and J. E. Cooper, "Clouds and the Earth's Radiant Energy System (CERES): An earth observing system experiment," *Bulletin of the American Meteorological Society*, vol. 77, no. 5, pp. 853–868, 1996.
- [17] J. Simpson, R. ADLER, and G. NORTH, "A proposed tropical rainfall measuring mission (TRMM) satellite," *American Meteorological Society, Bulletin*, vol. 69, pp. 278–295, 1988.
- [18] Miguel Roman and Charles K. Gatebe, "Interview at NASA GSFC on airborne BRDF products from past missions," 27-Jun-2012.
- [19] R. O. Green, M. L. Eastwood, C. M. Sarture, T. G. Chrien, M. Aronsson, B. J. Chippendale, J. A. Faust, B. E. Pavri, C. J. Chovit, M. Solis, and others, "Imaging spectroscopy and the airborne visible/infrared imaging spectrometer (AVIRIS)," *Remote Sensing of Environment*, vol. 65, no. 3, pp. 227–248, 1998.
- [20] D. A. Chu, Y. J. Kaufman, L. A. Remer, and B. N. Holben, "Remote sensing of smoke from MODIS airborne simulator during the SCAR-B experiment," *Journal of Geophysical Research*, vol. 103, no. D24, pp. 31979–31, 1998.
- [21] S. J. Hook, J. J. Myers, K. J. Thome, M. Fitzgerald, and A. B. Kahle, "The MODIS/ASTER airborne simulator (MASTER)—a new instrument for earth science studies," *Remote Sensing of Environment*, vol. 76, no. 1, pp. 93–102, 2001.

- [22] B. Cairns, L. D. Travis, and E. E. Russell, "The Research Scanning Polarimeter: calibration and ground-based measurements," in *Proc. SPIE*, 1999, vol. 3754, pp. 186–196.
- [23] P. Pilewski, J. Pommier, R. Bergstrom, W. Gore, S. Howard, M. Rabbette, B. Schmid, P. V. Hobbs, and S. C. Tsay, "Solar spectral radiative forcing during the southern African regional science initiative," *Journal of Geophysical Research*, vol. 108, no. D13, p. 8486, 2003.
- [24] D. J. Diner, L. M. Barge, C. J. Bruegge, T. G. Chrien, J. E. Conel, M. L. Eastwood, J. D. Garcia, M. A. Hernandez, C. G. Kurzweil, W. C. Ledebor, and others, "The Airborne Multi-angle Imaging SpectroRadiometer (AirMISR): instrument description and first results," *Geoscience and Remote Sensing, IEEE Transactions on*, vol. 36, no. 4, pp. 1339–1349, 1998.
- [25] S. Nag, C. K. Gatebe, and O. L. de Weck, "Nanosatellite clusters for multi-spectral, bi-directional reflectance distribution function estimations," in *Proceedings of the United Nations/Japan Nano-Satellite Symposium*, Nagoya, Japan, 2012.
- [26] W. Blackwell, G. Allen, C. Galbraith, T. Hancock, R. Leslie, I. Osaretin, L. Retherford, M. Scarito, C. Semisch, M. Shields, and others, "Nanosatellites for earth environmental monitoring: The MicroMAS project," in *Microwave Radiometry and Remote Sensing of the Environment (MicroRad), 2012 12th Specialist Meeting on*, 2012, pp. 1–4.
- [27] S. Satori, Y. Aoyanagi, U. Hara, R. Mitsuhashi, and Y. Takeuchi, "Hyperspectral sensor HSC3000 for nanosatellite TAIKI," in *Proceedings of SPIE, the International Society for Optical Engineering*, 2008, p. 71490M–1.
- [28] L. N. Phong and F. Ch[^]ateauneuf, "Nanosatellite distributed far infrared radiometers," in *Proc. SPIE*, 2009, vol. 7208, p. 72080L.
- [29] M. G. Mlynchzak, D. G. Johnson, M. N. Abedin, M. Stapelbroek, H. Hogue, and J. Reekstin, "The Far-Infrared Detector Technology Advancement Partnership-FIDTAP," *Passive Optical II*, 2006.
- [30] Alex Becerra, Marcos Diaz, and J.C. Zagal, "Feasibility study of using a Small Satellite constellation to forecast, monitor and mitigate natural and man-made disasters in Chile and similar developing countries."
- [31] 65 Authors from the Astronautics Community, *Space Mission Engineering: The New SMAD*, First. Microcosm Press, 2011.
- [32] Z. Jin, T. P. Charlock, K. Rutledge, K. Stamnes, and Y. Wang, "Analytical solution of radiative transfer in the coupled atmosphere-ocean system with a rough surface," *Applied optics*, vol. 45, no. 28, pp. 7443–7455, 2006.
- [33] E. Loewen and C. Palmer, *Diffraction Grating Handbook*. Newport Corporation, 2005.
- [34] J. Fraden, "Handbook of Modern Sensors: Physics, Designs, and Applications (*Handbook of Modern Sensors*), SpringerVerlag, 2003.
- [35] M. C. Gino, "Noise, noise, noise," <http://www.astrophys-assist.com/educate/noise/noise.htm>, 2002.
- [36] A. Barducci, D. Guzzi, P. Marcoionni, and I. Pippi, "CHRIS-Proba performance evaluation: signal-to-noise ratio, instrument efficiency and data quality from acquisitions over San Rossore (Italy) test site," in *Proceedings of the 3-rd ESA CHRIS/Proba Workshop, Italy*, 2005.
- [37] R. W. M. Hooegeveen, R. J. van der A, and A. P. H. Goede, "Extended wavelength InGaAs infrared (1.0–2.4 μm) detector arrays on SCIAMACHY for space-based spectrometry of the Earth atmosphere," *Infrared physics & technology*, vol. 42, no. 1, pp. 1–16, 2001.
- [38] H. Yuan, G. Apgar, J. Kim, J. Laquindanum, V. Nalavade, P. Beer, J. Kimchi, and T. Wong, "FPA development: from InGaAs, InSb, to HgCdTe," in *Proc. SPIE*, 2008, vol. 6940, p. 69403C.
- [39] G. A. Shaw and H. K. Burke, "Spectral imaging for remote sensing," *Lincoln Laboratory Journal*, vol. 14, no. 1, pp. 3–28, 2003.
- [40] R. F. Wolffenbuttel, "MEMS-based optical mini-and microspectrometers for the visible and infrared spectral range," *Journal of Micromechanics and Microengineering*, vol. 15, no. 7, p. S145, 2005.
- [41] R. F. Wolffenbuttel, "State-of-the-art in integrated optical microspectrometers," *Instrumentation and Measurement, IEEE Transactions on*, vol. 53, no. 1, pp. 197–202, 2004.
- [42] C. Ataman, H. Ürey, S. O. Isikman, and A. Wolter, "A MEMS based visible-NIR Fourier transform microspectrometer," in *Photonics Europe*, 2006, p. 61860C–61860C.
- [43] I. Powell and P. Cheben, "Modeling of the generic spatial heterodyne spectrometer and comparison with conventional spectrometer," *Applied optics*, vol. 45, no. 36, pp. 9079–9086, 2006.

- [44] S. Grabarnik, R. Wolffenbuttel, A. Emadi, M. Loktev, E. Sokolova, and G. Vdovin, "Planar double-grating microspectrometer," *Optics express*, vol. 15, no. 6, pp. 3581–3588, 2007.
- [45] P. Cheben, *Wavelength dispersive planar waveguide devices: echelle and arrayed waveguide gratings*, vol. 5. chapter, 2007.
- [46] Ti. Hewagama, S. Aslam, S. Talabac, J. E. Allen, J. N. Annen, and D. E. Jennings, "Miniature, Low-Power, Waveguide Based Infrared Fourier Transform Spectrometer for Spacecraft Remote Sensing," Jun. 2011.
- [47] N. K. Fontaine, K. Okamoto, T. Su, and S. J. B. Yoo, "Fourier-transform, integrated-optic spatial heterodyne spectrometer on a silica-based planar waveguide with 1?GHz resolution," *Opt. Lett.*, vol. 36, no. 16, pp. 3124–3126, Aug. 2011.
- [48] M. Florjańczyk, P. Cheben, S. Janz, A. Scott, B. Solheim, and D. X. Xu, "Spatial heterodyne planar waveguide spectrometer: theory and design," in *Proc. SPIE*, 2008, vol. 7099, p. 70991L.
- [49] J. A. Rodrigo, P. Cheben, T. Alieva, M. L. Calvo, M. Florjanczyk, S. Janz, A. Scott, B. Solheim, D. X. Xu, and A. Delàge, "Fresnel diffraction effects in Fourier-transform arrayed waveguide grating spectrometer," *Optics Express*, vol. 15, no. 25, pp. 16431–16441, 2007.
- [50] P. Cheben, I. Powell, S. Janz, and D. X. Xu, "Wavelength-dispersive device based on a Fourier-transform Michelson-type arrayed waveguide grating," *Optics letters*, vol. 30, no. 14, pp. 1824–1826, 2005.
- [51] M. Florjańczyk, P. Cheben, S. Janz, A. Scott, B. Solheim, and D. X. Xu, "Planar waveguide spatial heterodyne spectrometer," in *Proc. SPIE*, 2007, vol. 6796, p. 67963J–1.
- [52] K. Okamoto, "Progress and technical challenge for planar waveguide devices: silica and silicon waveguides," *Laser & Photonics Reviews*, vol. 6, no. 1, pp. 14–23, 2012.
- [53] J. M. Harlander, F. L. Roesler, C. R. Englert, J. G. Cardon, R. R. Conway, C. M. Brown, and J. Wimperis, "Robust monolithic ultraviolet interferometer for the SHIMMER instrument on STPSat-1," *Applied optics*, vol. 42, no. 15, pp. 2829–2834, 2003.
- [54] Y. Lin, G. Shepherd, B. Solheim, M. Shepherd, S. Brown, J. Harlander, and J. Whiteway, "Introduction to spatial heterodyne observations of water (SHOW) project and its instrument development," in *Proc. XIV Int. TOVS Study Conf*, 2005, pp. 25–31.
- [55] G. Georgiev, D. A. Glenar, and J. J. Hillman, "Spectral characterization of acousto-optic filters used in imaging spectroscopy," *Applied optics*, vol. 41, no. 1, pp. 209–217, 2002.
- [56] D. A. Glenar, J. J. Hillman, B. Saif, and J. Bergstralh, "Acousto-optic imaging spectropolarimetry for remote sensing," *Appl. Opt.*, vol. 33, no. 31, pp. 7412–7424, Nov. 1994.
- [57] J. Hillman, D. Glenar, D. M. Kuehn, and N. J. Chanover, "Compact Imaging Spectrometers using Acousto-Optic Tunable Filters," *The Weekly News Maganize of Science*, vol. 155, no. 3, pp. 26–30, 1999.
- [58] J. Vila-Francés, L. Gómez-Chova, J. Amorós-López, and J. Calpe-Maravilla, "Configurable Passband Imaging Spectrometer Based on Acousto-optic Tunable Filter," in *Proceedings of the 10th International Conference on Advanced Concepts for Intelligent Vision Systems*, Berlin, Heidelberg, 2008, pp. 206–217.
- [59] N. Gata, *Imaging spectroscopy using tunable filters: A review*, vol. 4056. Apr, 2000.
- [60] O. Korablev, J. L. Bertaux, A. Grigoriev, E. Dimarellis, Y. Kalinnikov, A. Rodin, C. Muller, and D. Fonteyn, "An AOTF-based spectrometer for the studies of Mars atmosphere for Mars Express ESA mission," *Advances in Space Research*, vol. 29, no. 2, pp. 143–150, 2002.
- [61] J. L. Bertaux, D. Nevejans, O. Korablev, E. Villard, E. Quémerais, E. Neefs, F. Montmessin, F. Leblanc, J. P. Dubois, and E. Dimarellis, "SPICAV on Venus Express: Three spectrometers to study the global structure and composition of the Venus atmosphere," *Planetary and Space Science*, vol. 55, no. 12, pp. 1673–1700, 2007.
- [62] N. J. Chanover, C. M. Anderson, C. P. McKay, P. Rannou, D. A. Glenar, J. J. Hillman, and W. E. Blass, "Probing Titan's lower atmosphere with acousto-optic tuning," *Icarus*, vol. 163, no. 1, pp. 150–163, 2003.
- [63] R. Bacon, G. Adam, A. Baranne, G. Courtes, D. Dubet, J. P. Dubois, E. Emsellem, P. Ferruit, Y. Georgelin, and G. Monnet, "3D spectrography at high spatial resolution. I. Concept and realization of the integral field spectrograph TIGER," *Astronomy and Astrophysics Supplement Series*, vol. 113, p. 347, 1995.
- [64] M. A. Peters, T. Groff, N. J. Kasdin, M. W. McElwain, M. Galvin, M. A. Carr, R. Lupton, J. E. Gunn, G. Knapp, and Q. Gong, "Conceptual design of the coronagraphic high angular resolution imaging spectrograph (charis) for the subaru telescope," in *SPIE Astronomical Telescopes+ Instrumentation*, 2012, p. 84467U–84467U.

- [65] M. W. McElwain, T. D. Brandt, M. Janson, G. R. Knapp, M. A. Peters, A. Burrows, A. Carlotti, M. A. Carr, T. Groff, and J. E. Gunn, "Scientific design of a high contrast integral field spectrograph for the subaru telescope," in *Proc. of SPIE Vol.*, 2012, vol. 8446, p. 84469C–1.
- [66] C. K. Gatebe, J. J. Butler, J. W. Cooper, M. Kowalewski, and M. D. King, "Characterization of errors in the use of integrating-sphere systems in the calibration of scanning radiometers," *Applied optics*, vol. 46, no. 31, pp. 7640–7651, 2007.
- [67] S. Kodama, M. Ohtake, Y. Yokota, A. Iwasaki, J. Haruyama, T. Matsunaga, R. Nakamura, H. Demura, N. Hirata, and T. Sugihara, "Characterization of Multiband Imager Aboard SELENE," *Space science reviews*, vol. 154, no. 1, pp. 79–102, 2010.
- [68] J. S. Pearlman, P. S. Barry, C. C. Segal, J. Shepanski, D. Beiso, and S. L. Carman, "Hyperion, a space-based imaging spectrometer," *Geoscience and Remote Sensing, IEEE Transactions on*, vol. 41, no. 6, pp. 1160–1173, 2003.
- [69] J. J. Butler, X. Xiong, R. A. Barnes, F. S. Patt, J. Sun, and K. Chiang, "An overview of Suomi NPP VIIRS calibration maneuvers," in *SPIE Optical Engineering+ Applications*, 2012, p. 85101J–85101J–13.
- [70] M. Ohtake, J. Haruyama, T. Matsunaga, Y. Yokota, T. Morota, C. Honda, and L. Team, "Performance and scientific objectives of the SELENE (KAGUYA) Multiband Imager," *Earth Planets and Space (EPS)*, vol. 60, no. 4, p. 257, 2008.
- [71] C. Bruegge, N. Chrien, and D. Haner, "A Spectralon BRF data base for MISR calibration applications," *Remote sensing of environment*, vol. 77, no. 3, pp. 354–366, 2001.
- [72] C. J. Bruegge, A. E. Stiegman, R. A. Rainen, and A. W. Springsteen, "Use of Spectralon as a diffuse reflectance standard for in-flight calibration of earth-orbiting sensors," *Optical Engineering*, vol. 32, no. 4, pp. 805–814, 1993.
- [73] G. B. Courreges-Lacoste, J. G. Schaarsberg, R. Sprik, and S. Delwart, "Modeling of Spectralon diffusers for radiometric calibration in remote sensing," *Optical engineering*, vol. 42, no. 12, pp. 3600–3607, 2003.
- [74] G. T. Georgiev and J. J. Butler, "Long-term calibration monitoring of Spectralon diffusers BRDF in the air-ultraviolet," *Applied optics*, vol. 46, no. 32, pp. 7892–7899, 2007.
- [75] G. Minelli, A. Ricco, and C. O. Kitts, "O/oreos nanosatellite: A multi-payload tech-nology demonstration," in *Proceedings of the 24th Annual AIAA/USU Conference on Small Satellites*, 2010.
- [76] C. J. Leising, B. Sherwood, M. Adler, R. R. Wessen, and F. M. Naderi, "Recent improvements in JPL's mission formulation process," in *Aerospace Conference, 2010 IEEE*, 2010, pp. 1–12.
- [77] T. N. Krabach, C. Staller, S. Dejewski, T. Cunningham, M. Herring, and E. R. Fossum, "InGaAs detectors for miniature infrared instruments," in *SPIE*, 1993, vol. 1874, pp. 214–223.